J. Fluid Mech. (1993), *vol.* 246, *pp.* 613–652

Dynamical aspects of vortex reconnection of perturbed anti-parallel vortex tubes

By M. J. SHELLEY,[1] D. I. MEIRON[2] AND S. A. ORSZAG[3]

[1] Computational and Applied Mathematics Program, Department of Mathematics, University of Chicago, Chicago, IL 60637, USA

[2] Applied Mathematics, California Institute of Technology, Pasadena, CA 91125, USA

[3] Program in Applied and Computational Mathematics, Princeton University, Princeton, NJ 08544, USA

(Received 1 November 1990 and in revised form 31 July 1992)

The phenomenon of vortex reconnection is analysed numerically and the results are compared qualitatively with the predictions of a model of reconnection recently proposed by Saffman. Using spectral methods over both uniform and strained meshes, numerical simulations are performed of two nearly parallel, counter-rotating vortex tubes, over the range of Reynolds numbers $Re = 1000$–3500. The calculations utilizing a uniform mesh are performed for $Re \leqslant 1500$ with a resolution of 128 points in each direction. The calculations utilizing a stretched mesh are performed for $1500 < Re \leqslant 3500$ with a resolution of up to 160 points in each direction and with a fourfold stretching about the region of reconnection. We present results for the variation of the maximum of vorticity, the time to reconnection, and other diagnostics of this flow as functions of the Reynolds number. From numerical simulation of the model equations, we infer and demonstrate the existence of exact solutions to the model to which its solutions arising from more general initial conditions are attracted at late times. In the limit of infinite Reynolds number, the model predicts eventual saturation of the axial strain, a feature observed in the recent work of Pumir & Siggia and also observed in our full numerical simulations. In this respect the model captures the observed local dynamics of vortex stretching. However, because the global effects of external flows are not included in the model, the model predicts that the axial strain eventually decays and the maximum vorticity grows linearly at late times. In contrast, from the full simulations, we see the possible emergence of the behaviour of the axial strain at infinite Reynolds number. As our simulations are affected by non-local effects, we do observe saturation of the strain but no subsequent decay. It is also shown analytically that the model predicts a reconnection time which varies logarithmically with increasing Reynolds number. Comparison with the full numerical simulations shows a much slower variation of the reconnection time with increasing Reynolds number than predicted by the model. Other points of agreement and disagreement between the Saffman model and the simulations are discussed. Reconnection is also discussed from the point of view of its relation to the possible onset of nearly singular behaviour of the Euler equation. In agreement with the recent numerical results of Pumir & Siggia, our results suggest that no singularity in the vorticity will form in a finite time for this initial condition.

1. Introduction

The phenomenon of vortex reconnection has become a topic of considerable research interest in recent years. The phenomenon is often observed in aircraft contrails, and has been reproduced in numerous laboratory experiments and numerical simulations. Crow (1970) was the first to analyse the initial instability which leads to reconnection in which sections of counter-rotating tubes pair and stretch. In the late stages of this instability the paired portions of the tubes seem to annihilate and the tubes are transformed into a series of vortex rings. Pictures of the phenomenon can be found in the album assembled by Van Dyke (1982). Experimental measurements of it have been performed by Fohl & Turner (1975), Oshima & Asaka (1977), and recently by Schatzle (1987), who has made velocity measurements of two colliding vortex rings by means of laser Doppler anemometry. Numerical simulations have been performed by Ashurst & Meiron (1987), Kida (1987), Kerr & Hussain (1989), Meiron *et al.* (1989), Melander & Hussain (1989), Melander & Zabusky (1989), Anderson & Greengard (1989), Kida & Takaoka (1991), and others.

The phenomenon of reconnection is of interest from both a physical and mathematical point of view. Reconnection can only occur in the presence of viscous dissipation. The Helmholtz theorems indicate that in the absence of viscosity, all incompressible velocity fields can be viewed as arising from a collection of infinitesimal vortex filaments. These filaments can be shown to be material with the flow, so that the identity of each filament is preserved under the flow. In addition, since the vorticity field is divergence-free, the filament must be of infinite extent or close on itself in the absence of boundaries. In order to break these constraints some dissipative mechanism such as fluid viscosity must be operative. The reconnection process exemplifies the dynamical effects of viscosity at short lengthscales in flows of high Reynolds number.

Reconnection may also play a role in the mathematical theory of long-time existence of bounded solutions to the three-dimensional Navier–Stokes and Euler equations. There is at present no rigorous proof that, given a smooth velocity field as initial data, velocity gradients will stay bounded for all time under the evolution of either equation. Numerical simulations have not been able to resolve this issue. For example, the numerical work of Brachet *et al.* (1983) examined the dynamics of the Taylor–Green vortex, an initial condition possessing a high degree of symmetry which is preserved under the dynamics of both the Euler and Navier–Stokes equations. Earlier work by Morf, Orszag & Frisch (1980) using series analysis techniques indicated the possible existence of a singularity in finite time for this flow, but further series work and numerical simulations did not lead to a confirmation of singular behaviour. Indeed, the later numerical evidence of Brachet *et al.* favoured the interpretation that singularities were not present for these initial conditions even in the limit of zero viscosity.

For the Euler equations, there are constraints on the character of the singular set. Beale, Kato & Majda (1984) have shown that if there exists a time, t^*, at which a solution loses any regularity, then it must be that the maximum of the vorticity magnitude over the flow domain becomes unbounded, i.e.

$$\lim_{t \to t^*} \|\omega\|_\infty(t) = \infty, \tag{1.1}$$

and that, moreover,

$$\lim_{t\to t^*}\int_0^{t^*}\|\omega\|_\infty(t)\,\mathrm{d}t=\infty. \tag{1.2}$$

Equation (1.2) provides a constraint on how the vorticity must diverge. For example, a divergence such as

$$\|\omega\|_\infty(t)=\frac{C}{(t^*-t)^{\frac{1}{2}}} \tag{1.3}$$

is disallowed by (1.2). From physical considerations, it is natural to expect that the presence of viscosity should restore boundedness and that the Navier–Stokes equations should possess regular solutions for all time. But even this has not been proven.

Grauer & Sideris (1991) have recently reported finite-difference simulations of an inviscid axisymmetric flow with swirl and claim that a singularity occurs after a finite time t^* and its growth is consistent with the theoretical results of Beale *et al.* (1984). However, no specific rate of divergence is given. The possibility that this kind of singular vortex growth occurs in these constrained flows requires much further study, and in particular, careful numerical tests of accuracy to rule out numerically induced instabilities. However, a singularity which may not be possible without constraints may be possible for the Grauer & Sideris flow because the flow cannot 'wriggle' its way out of singularity formation.

The physical characteristics of flow near a singularity are also poorly understood. A prevailing hypothesis discussed, for example, in the work of Brachet *et al.* (1983) was that the vortex lines of the flow near a singularity were highly convoluted, of infinite length and therefore fractal in nature. A similar belief underscores the work of Chorin (1981). A quite different physical picture was proposed by Siggia (1985) and Siggia & Pumir (1987). They have modelled the interaction of vortex tubes as the flow resulting from the close interaction of oppositely signed vortex filaments and have shown that vortex stretching in such a flow may lead to a singularity in finite time. The results suggest a scenario for singularity quite different from those which involve complicated tangling of the vortex lines. Within the context of the filament model, Siggia & Pumir also indicated that even under the Navier–Stokes equations, large but not divergent velocities could be produced.

The use of filaments constitutes an acceptable approximation to the solution of the Euler equations only under certain conditions. The conclusions of Siggia & Pumir (1987) on the near singularity of the Navier–Stokes equations (and also on the singularity of the Euler equations) depend crucially on the assumption that the circular cores of the vortex tubes which are modelled as filaments do not deform appreciably as the tubes interact. Such considerations will also play a role in any analysis of reconnection, particularly in the limit of high Reynolds number. For example, Pumir & Kerr (1988) observed substantial deformation of the cores in their numerical simulations. Later numerical calculations by Pumir & Siggia (1990) indicate that the deformation of the vortex cores effectively prohibits unbounded growth of the vorticity. Thus deformation can also be expected to play an important role in reconnection as well.

In this work we examine several models of the reconnection process. Each of these models makes assumptions on the flow geometry in order to obtain analytical estimates of flow quantities. In §1.1 we review the Siggia–Pumir model of singularities in the context of reconnection. We then examine in §1.2 models which attempt to build in the effects of vortex deformation. The first model was proposed by Kambe (1983) and attempts to incorporate the effect of in-plane strains on the structure of the vortices. Buntine & Pullin (1989) modified Kambe's model to include the effects of axial, out-of-plane strain. Recently, Saffman (1990) has proposed a model which incorporates out-of-plane strains (and hence vortex stretching) in a partially self-consistent manner by considering the axial pressure gradients in the cores of the reconnecting tubes. In this paper we show that Saffman's model possesses simple analytical solutions which describe the long-time dynamics of the model. Numerical studies of the Saffman model are described in §2.2. The numerics demonstrate the existence of these simple analytical solutions, valid at late times, and the solutions are derived in §2.3.

In order to assess the validity of these models we also perform full numerical simulations of the flow of two oppositely signed vortex tubes and their subsequent reconnection under the Navier–Stokes equations. Our goal here is to provide quantitative estimates of the deformation of the vortex cores, the amplification of vorticity, and the timescale for reconnection. The simulations utilize a standard pseudo-spectral method as well as an adaptive spectral method which provides enhanced resolution in specified regions of physical space. The two numerical methods are described in §3.1. The initial conditions considered here have symmetries that are preserved by the ensuing flow, and these symmetries are exploited to reduce the computational work. These are described in §3.2. The results of the numerical simulations are described in §§3.3 and 3.4. These calculations are carried out at moderate Reynolds numbers, but are valuable in indicating the physical processes which cause the deformation of the vortices. As the Reynolds number is increased, we see the emergence of behaviour in certain quantities which may be independent of the Reynolds number and hence represents the limit of infinite Reynolds number. We observe here, in agreement with the numerical calculations of Pumir & Siggia (1990) and Anderson & Greengard (1989), that the axial strain initially increases, causing vortex stretching, but the deformation of the vortex cores eventually causes the saturation of the strain, and thus we infer that the vorticity will not become unbounded in a finite time for this flow.

1.1. *Siggia–Pumir model for singularities*

Given a distribution of vorticity $\boldsymbol{\omega}(x,y,z,t)$, it is possible to construct the flow velocity $\boldsymbol{v}(x,y,z,t)$ by means of the Biot–Savart law:

$$\boldsymbol{v}(x,y,z,t) = -\frac{1}{4\pi}\int_V \mathrm{d}V'\,\frac{\boldsymbol{\omega}(x',y',z',t)\times(\boldsymbol{r}-\boldsymbol{r}')}{|\boldsymbol{r}-\boldsymbol{r}'|^{\frac{3}{2}}}, \tag{1.4}$$

where the integration extends over the support V of the vorticity $\boldsymbol{\omega}$. Alternatively, one may view $\boldsymbol{v}(x,y,z,t)$ as that velocity arising from a continuous distribution of vortex filaments. If the velocity distribution takes the form of an isolated filament then (1.4) simplifies to

$$\boldsymbol{v}(x,y,z,t) = -\frac{1}{4\pi}\int \mathrm{d}\xi'\,\Gamma(\xi')\,\frac{[\boldsymbol{r}-\boldsymbol{r}(\xi')]\times\mathrm{d}\boldsymbol{r}/\mathrm{d}\xi'}{|\boldsymbol{r}-\boldsymbol{r}(\xi')|^{\frac{3}{2}}}, \tag{1.5}$$

where Γ is the circulation of the vortex filament and ξ is a Lagrangian variable used to parameterize the filament. If the vorticity is concentrated within a thin tube then the velocity given by (1.5) serves as an approximation for the velocity given by (1.4). It will not, however, provide a uniformly valid approximation. The integral in (1.5) diverges logarithmically if $\boldsymbol{r}$ is set to be any point along the filament. This is simply a reflection of the fact that (1.5) would represent only the first term in a multipole expansion for the velocity produced by any vorticity distribution with net circulation

Γ. Such an expression gives sensible velocities provided that the observation point $\boldsymbol{r}$ is sufficiently far from the filament relative to some typical core size for the vorticity distribution. In order to regularize the velocity given by (1.5), the core structure can be taken into account in an approximate way by introducing a core length $\sigma(\xi)$ which in general varies along the filament and rewriting (1.5) as

$$\boldsymbol{v}(x,y,z,t) = -\frac{1}{4\pi}\int \mathrm{d}\xi' \, \Gamma(\xi') \frac{[\boldsymbol{r}-\boldsymbol{r}(\xi')] \times \mathrm{d}\boldsymbol{r}/\mathrm{d}\xi'}{[|\boldsymbol{r}-\boldsymbol{r}(\xi')|^2+\sigma^2(\xi')]^{\frac{3}{2}}}. \tag{1.6}$$

Since (1.6) now provides a finite velocity field, we may now apply the Helmholtz laws to give a prescription for the motion of the vortex filament $\boldsymbol{r}(\xi,t)$ according to

$$\mathrm{d}\boldsymbol{r}(\xi,t)/\mathrm{d}t = \boldsymbol{v}(\xi), \tag{1.7}$$

where $\boldsymbol{v}(\xi)$ is the velocity obtained from (1.6) by setting $\boldsymbol{r}$ to $\boldsymbol{r}(\xi)$. In using (1.6) to provide an advection velocity for the filament we are failing to account for the contribution to the velocity which is due to the finite core size. This approximation completely ignores, for example, internal flows within the core.

It is possible to incorporate some aspects of the true core phenomena given by (1.4) into (1.6). For example, in calculations using ring filaments it is possible to adjust σ such that it gives the correct velocity of advance for a vortex ring of a given radius and vorticity distribution. In numerical simulations in which filaments are stretched, the conservation of tube volume under the flow which is a consequence of the Helmholtz laws can be approximated through the condition

$$\sigma^2(\xi)\,|\mathrm{d}\boldsymbol{r}/\mathrm{d}\xi| = \text{constant}. \tag{1.8}$$

Equation (1.8) is only one of many possible 'core laws' which express conservation of tube volume. Combined with the equation

$$\mathrm{d}\boldsymbol{r}(\xi)/\mathrm{d}t = \boldsymbol{v}(\xi), \tag{1.9}$$

(1.6) and (1.8) form a closed system which may be used to numerically compute the evolution of the filament.

Siggia & Pumir (1987) have performed careful simulations using this set of equations, and have shown convincingly that an isolated filament can fold upon itself such that oppositely signed pieces of the filament pair advance under their mutual velocity fields and cause stretching of the filament. Because of the constraint of volume conservation, the core size will shrink as the filament stretches. A typical velocity scale along the filament for a given core size σ from the Biot–Savart law is

$$|\boldsymbol{v}| \sim \Gamma/\sigma, \tag{1.10}$$

while a typical vorticity scale is

$$|\boldsymbol{\omega}| \sim \Gamma/\sigma^2. \tag{1.11}$$

Thus if the core size reduces to zero in a finite time, the filament model predicts that the velocity and vorticity will both diverge. For the Euler equation, the constraint of energy conservation effectively forbids a velocity singularity that has a finite spatial support but pointwise divergence cannot be ruled out. The results of Siggia & Pumir indicate that the stretching is so rapid that the core size reduces to zero in a finite time, leading to a divergent vorticity.

By taking the constant in (1.8) to be unity and differentiating with respect to time, (1.8) becomes

$$\frac{\mathrm{d}\sigma^2}{\mathrm{d}t} = -\sigma^2\frac{\mathrm{d}}{\mathrm{d}t}\ln\left(\frac{\mathrm{d}s}{\mathrm{d}\xi}\right), \tag{1.12}$$

where $\mathrm{d}s/\mathrm{d}\xi = |\mathrm{d}\boldsymbol{r}/\mathrm{d}\xi|$. As a filament pairs, Siggia & Pumir observe that the stretching is so rapid that the decrease of the interfilament spacing is directly correlated with the decrease of the core size. This is due to the straining flow set up by the filament pair. Using this information, Siggia & Pumir estimated the right-hand side of (1.12) to be

$$\frac{\mathrm{d}}{\mathrm{d}t}\ln\left(\frac{\mathrm{d}s}{\mathrm{d}\xi}\right) \sim \frac{\Gamma}{\sigma^2}. \tag{1.13}$$

Once the rapid stretching ensues the core behaves according to the relation

$$\mathrm{d}\sigma^2/\mathrm{d}t \propto -\Gamma \tag{1.14}$$

or

$$\sigma \sim [\Gamma(t^* - t)]^{\frac{1}{2}}. \tag{1.15}$$

The collapse of the core is self-similar in that only the core size and the timescale are involved in the local enforcement of conservation of circulation. Such a divergence is consistent with the theoretical constraints given in (1.1) and (1.2).

There are several difficulties with this scenario for a finite-time singularity. A filament description is certainly questionable when applied at such small length-scales. Since the cores are constrained to be circular it is possible for the cores to overlap in this model. Indeed, it is observed that the interfilament spacing decreases to a fraction of the core size once the collapse begins indicating overlap of the cores. Siggia & Pumir (1987) showed that the singular scaling laws predicted from their filament model could be expected to hold provided that the circular cores do not deform appreciably. Their later calculations showed that the cores do deform and no analytical estimate is currently available for the effect of the deformation on the filament velocity.

An additional physical effect which is not included in a simple filament model is the effect of axial flows along the tube. Models have been constructed by Moore & Saffman (1972) and Lundgren & Ashurst (1988) which model the effect of the swirling flows in the core on the dynamics of the tube. In such models the core law (1.8) is used along with equations of motion for the axial velocity. These models continue to assume that the cores are circular but account for the presence of waves travelling along the core which can redistribute the core area along the filament. Numerical studies due to Lundgren & Ashurst (1988) show, however, that this effect will not impede the collapse provided that the cores are circular. The maximum velocity generated in the collapse exceeds the maximum phase speed of the axial waves by a constant factor. Thus while the timescale for the collapse is changed, the finite time singularity in this enhanced filament model remains.

One can show from the above considerations that in the presence of viscosity the Siggia–Pumir model leads to a reconnection time which is independent of the Reynolds number as $Re \rightarrow \infty$. As the vortex tubes approach, one can crudely model the decay of the circulation by

$$\mathrm{d}\Gamma/\mathrm{d}t = -(1/Re)\,\Gamma/\delta^2, \tag{1.16}$$

where δ is the separation between the vortex cores. Assuming that $\delta \approx \sigma$ as the vortices enter a singular configuration we model the variation of δ by

$$\mathrm{d}\delta^2/\mathrm{d}t = -\Gamma, \tag{1.17}$$

which, in the absence of viscosity leads to the Siggia–Pumir collapse. Solving (1.16) and (1.17), one obtains the relation

$$\delta^2(t) = \exp\left(Re\,(\Gamma(t) - 1)\right), \tag{1.18}$$

where the initial separation and circulation are taken to be one. As t increases, the circulation remains virtually constant until the singularity time, which is given by $t^* = 1$ in these units. At this time, in the presence of viscosity, the circulation rapidly drops to zero leaving a separation which is constant in time. Thus viscosity regularizes this singularity. However, the separation can still become very small. For example, if we define the reconnection time t_R as that time needed to decrease the circulation to one half its initial value then it can be shown that

$$t_R \sim 1 + O(1/Re).$$

At this time from (1.18) we have

$$\delta \approx \exp(-\tfrac{1}{2} Re\, \Gamma).$$

The velocities near this time are enormous since they scale as Γ/δ. Thus the Siggia–Pumir model predicts a reconnection time which decreases with increasing Re and tends to a finite limit as it must since a singularity develops.

Clearly, these estimates will depend strongly on the deformation of the vortex. At present no self-consistent model for vortex deformation and its effect on stretching is available. Below we discuss several attempts to model the deformation.

1.2. *Modelling of vortex deformation*

1.2.1. *Kambe's model*

Kambe (1983) has shown that if two oppositely signed shear layers in the plane are driven together by a straining flow, destruction or cancellation of vorticity can take place on a nearly convective timescale which increases very slowly with increasing Reynolds number and scales inversely with the rate of strain of the flow. Following Kambe we consider a two-dimensional flow of the form

$$u = -\alpha(t)\, x, \quad v = \alpha(t)\, y + V(x,t). \tag{1.19}$$

Such a velocity field represents the action of an external, irrotational strain flow on a region of vorticity which varies only with x. The vorticity $\boldsymbol{\omega}$ is directed along the z-axis and is given by

$$\boldsymbol{\omega} = \omega \boldsymbol{k} = (\partial V/\partial x)\, \boldsymbol{k}. \tag{1.20}$$

The vorticity equation for this flow becomes

$$\partial\omega/\partial t - \alpha(t)\, x\, \partial\omega/\partial x = \nu\, \partial^2\omega/\partial x^2. \tag{1.21}$$

Using the scaling
$$\xi = B(t)\, x, \quad \tau = \int_0^t \mathrm{d}t' B(t')^2, \tag{1.22}$$

where
$$B(t) = \exp A(t), \quad A(t) = \int_0^t \mathrm{d}t' \alpha(t'), \tag{1.23}$$

the vorticity equation becomes the heat equation in a stretched coordinate system:

$$\partial\omega/\partial\tau = \nu\, \partial^2\omega/\partial\xi^2. \tag{1.24}$$

For $\alpha(t)$ constant we have

$$\xi = \exp(\alpha t)\, x, \quad \tau = 1/2\alpha[\exp(2\alpha t) - 1]. \tag{1.25}$$

Kambe considered the evolution of a shear layer with an initial distribution of vorticity given by

$$\omega(x, t=0) = U[\delta(x + x_0) - \delta(x - x_0)], \tag{1.26}$$

where $\delta(x)$ is the usual Dirac δ-function. Such an initial condition models a highly elongated vorticity distribution. Using dimensionless variables, in which lengths are scaled by x_0 and velocities by U, the solution of (1.24) with initial data (1.26) is

$$\omega(\xi,t)=\frac{1}{(T(t))^{\frac{1}{2}}}\left[\exp\left(-\frac{(\xi+1)^2}{T(t)}\right)-\exp\left(-\frac{(\xi-1)^2}{T(t)}\right)\right], \tag{1.27}$$

where

$$T(t)=(2/Re)[\exp(2\alpha t)-1] \tag{1.28}$$

and Re, the Reynolds number is given by $Re=Ux_0/\nu$. For large values of the Reynolds number the peaked structure of the vorticity is maintained until $T(t)$ increases to be $O(1)$. For α constant this occurs at a characteristic reconnection time t_R given by

$$t_R \sim \ln Re/(2\alpha). \tag{1.29}$$

In contrast with the result obtained from the Siggia–Pumir model this timescale increases very slowly with increasing Re. Thus, the reconnection process as modelled by Kambe is fairly rapid even at large values of the Reynolds number, but the result also mirrors the underlying existence of the inviscid flow field for all time. Kambe's model is not self-consistent in that the in-plane strain is imposed and is not coupled to the vorticity. Moreover, the imposed strain is two-dimensional.

1.2.2. *Model of Buntine & Pullin*

Attempting to improve upon Kambe's model of reconnection, Buntine & Pullin (1989) studied the effect of a specified out-of-plane straining flow on the dynamics of the vorticity and its subsequent decay. In particular, they studied flow fields of the form

$$u=-\alpha(t)\,x+\hat{u}(x,y,t), \tag{1.30}$$

$$v=[\alpha(t)-\beta(t)]\,y+\hat{v}(x,y,t), \tag{1.31}$$

$$w=\beta(t)\,z+\hat{w}(x,y,t). \tag{1.32}$$

For such flow fields, w is a passive and diffusing field, whose only effect on the two-dimensional field (u,v) is through the specified strain rate $\beta(t)$. The evolution for the z-component of vorticity ω is given by

$$\frac{\partial\omega}{\partial t}+u\frac{\partial\omega}{\partial x}+v\frac{\partial\omega}{\partial y}=\beta(t)\,\omega+\nu\nabla^2\omega. \tag{1.33}$$

Buntine & Pullin repeated Kambe's analysis with smooth initial vorticity distributions but similar in form to (1.26). For positive and constant α and β they found that the circulation is determined asymptotically in time solely by the strain rate α as

$$\Gamma(t)\sim C(\alpha Re)^{\frac{1}{2}}\,\mathrm{e}^{-\alpha t}, \tag{1.34}$$

which for large Re yields the same timescale for reconnection as that given by Kambe. That is, asymptotically the stretching of the vortices by out-of-plane strain does not influence circulation destruction in this model.

Buntine & Pullin also computed the pressure drop at the vortex centre and showed that it agrees well with the pressure drop as computed by Moore & Saffman (1971) for an elliptical (Kirchhoff) vortex in a straining flow. This is remarkable in the light of the fact that the Moore–Saffman result is derived from an equilibrium solution of the Euler equations. This observation is used by Saffman in his construction of the model of reconnection described below.

2. Saffman model of reconnection

In recent work, Saffman (1990) has attempted to partially couple the strain flows to the vorticity distribution. He posed a set of nonlinear partial differential equations to describe the approach of two vortices, as well as their subsequent core deformation, stretching, and diffusion. Saffman presents the model equations and some preliminary numerical results together with some conjectures on the timescales predicted by the model for core deformation and for reconnection. Here we will show that the asymptotic behaviour of the model can be understood completely in terms of the behaviour of special solutions of the model equations. From these solutions we derive an asymptotic estimate for the timescale for reconnection. It will be seen that Saffman's model predicts an eventual decay of the axial out-of-plane strain as the vortex cores flatten, leading once again to a timescale for reconnection which is proportional to log (*Re*) and inversely proportional to the in-plane strain rate α. The model also predicts, in the absence of viscosity, that the vorticity will ultimately grow through mutually induced stretching at only a linear rate. A linear rate of growth of the vorticity has been observed in the work of Anderson & Greengard (1989). On the other hand, Pumir & Siggia (1990) observe exponential growth at late times. We now turn to a discussion of Saffman's model.

2.1. *Equations of motion*

Referring to the schematic in figure 1, we consider the motion of two counter-rotating vortex tubes that are merging about $z = 0$. Note that figure 1 shows merging about $z = \pi$. This exact configuration will be discussed later in connection with the numerical solution. For the purposes of this discussion however, we simply translate the z-coordinate by π. It is assumed that the irrotational strain field in this region is given by

$$u = -[\alpha+\beta(z,t)]\,x, \quad v = \alpha y, \quad w = \int_0^z \beta(z',t)\,\mathrm{d}z'. \tag{2.1}$$

An estimate for the rate of strain α is obtained by considering the in-plane strain arising in the plane of closest approach of two vortices shown in figure 1 and is given by

$$\alpha = k\Gamma_0/R^2, \tag{2.2}$$

where R is the initial radius of curvature of the tube at $z=0$, Γ_0 is the initial circulation, and k an undetermined constant set by the geometry. The evolution of the axial strain, $\beta(z,t)$, is determined from the balance of axial momentum.

Let $\delta(z,t)$ denote the distance between the core centroids, and $b(z,t)$ and $h(z,t)$ the minor and major semi-axes of the deformed cores. Saffman models the evolution of the centroid position and the core area bh of the vortices by the convection–diffusion equations

$$\partial\delta/\partial t = -(\alpha+\beta)\,\delta+\nu'/\delta, \tag{2.3}$$

$$\partial(bh)/\partial t = -\beta(bh)+\nu'. \tag{2.4}$$

Here ν' is proportional to the kinematic viscosity ν and, following Saffman, is given by $\nu' = 2\pi\nu$. The vortex cores have circulations $\pm\Gamma(z,t)$. The decay of the circulation is modelled by

$$\partial\Gamma/\partial t = -\nu'\Gamma/\delta^2. \tag{2.5}$$

Saffman now models the z-momentum equation by

$$\partial w/\partial t = -\partial p/\partial z - w\,\partial w/\partial z, \tag{2.6}$$

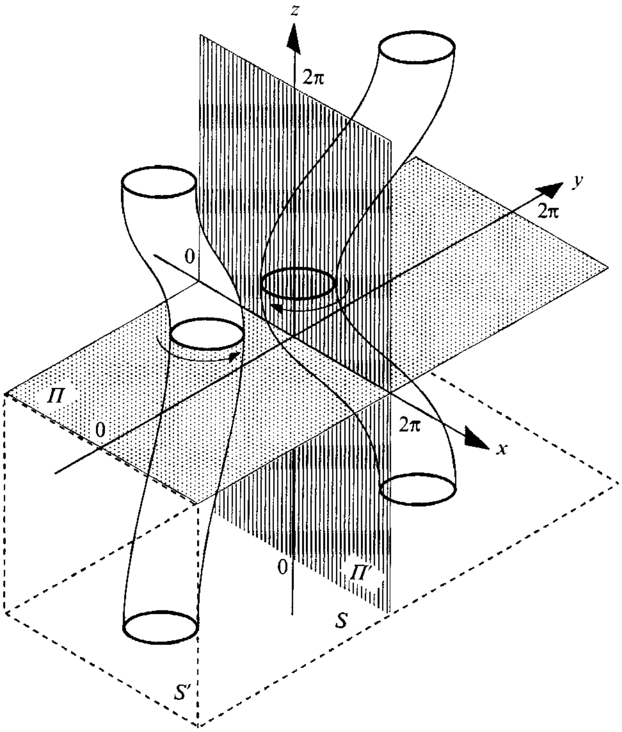

FIGURE 1. Geometric configuration of two vortices of opposite circulation.

where w and p are average axial velocities and pressures over the cores. The rate of strain β may now be determined from the axial velocity:

$$\beta(z,t) = (\partial w/\partial z)(z,t). \tag{2.7}$$

We now lack only an expression for the pressure p, which is assumed to depend upon the core deformation. Using the observations of Buntine & Pullin (1989) on the evolution of strained vortices, the pressure is modelled by the expression

$$p = \frac{-\Gamma^2}{2\pi^2 bh} f(\theta), \tag{2.8}$$

where $\theta = h/b$ is the axis ratio, and

$$f(\theta) = \theta/(1+\theta^2). \tag{2.9}$$

The aspect ratio θ is given by

$$\theta = 1+4r \quad \text{with} \quad r = \pi\alpha bh/\Gamma + bh/\delta^2. \tag{2.10}$$

These expressions originate from a calculation of the pressure drop at the centre of a Kirchhoff elliptical vortex which is held steady by a given straining flow (Moore & Saffman 1971). We refer the reader to Saffman (1990) for further details concerning the derivation. We note however that the model effectively fixes the aspect ratios of the elliptical vortex cores once their separation, δ, and area, A, are given. In this respect, it cannot be compared directly with numerical simulations which pose both aspect ratio and separation as initial conditions. Rather, the initial conditions of this model should be interpreted as some appropriate intermediate configuration which has been reached.

The essential idea as stated by Saffman is that in the plane of closest approach, cancellation of vorticity by viscosity, will raise pressures in the vortex cores. This yields a pressure gradient and drives axial flows which then complete the reconnection. It should be pointed out, however, that given the use of elliptical vortices and the related formula for the pressure given above, axial flows are set up *independently* of the viscosity. Thus the model also makes predictions in the limit $\mu \rightarrow 0$. We elaborate on this point below.

The equations of motion are now closed, with four equations of evolution for the four unknowns α, $A = bh$, Γ, and w. After appropriate scalings of the dependent variables, these equations, in non-dimensional form are

$$\partial\delta/\partial t = -(\epsilon^{\frac{3}{2}} + \partial w/\partial z)\,\delta + \mu/\delta, \tag{2.11}$$

$$\partial A/\partial t = -(\partial w/\partial z)\,A + \mu, \tag{2.12}$$

$$\partial \Gamma/\partial t = -\mu\,\Gamma/\delta^2, \tag{2.13}$$

$$\partial w/\partial t = -w\,\partial w/\partial z - \partial p/\partial z, \tag{2.14}$$

where

$$p = -f\Gamma^2/(2A), \quad f(\theta) = \theta/(1+\theta^2),$$

and

$$\theta = 1+4r \quad \text{with} \quad r = \epsilon^2 A/\Gamma + A/\delta^2.$$

Here, $\epsilon = a/R$ is the ratio of the core size of the vortices to the radius of curvature of the vortex tube, and

$$\mu = \nu'\pi/(\Gamma_0\,\epsilon^{\frac{1}{2}})$$

is an inverse Reynolds number. The dimensional space and time variables, z^*, t^* are given by

$$z^* = \epsilon^{-\frac{1}{2}}\alpha z, \quad t^* = \epsilon^{\frac{3}{2}} t/\alpha.$$

Following Saffman we have set $k = 1/\pi$ for definiteness.

Below we present numerical results in addition to those presented by Saffman. It will be seen from these results that Saffman's model predicts an eventual decay of the axial out-of-plane strain as the vortex cores flatten. This leads once again to a timescale for reconnection similar to that given in (1.29). We also show that the asymptotic behaviour of the model can be understood in terms of the behaviour of special solutions of the model equations. From these solutions we derive an asymptotic estimate for the reconnection timescale.

2.2. *Numerical solution*

We have solved these equations numerically for the initial conditions

$$\delta(z, t=0) = 2 + \frac{2}{(2\pi/L)^2} - \frac{2}{(2\pi/L)^2}\cos(2\pi/L)\,z, \tag{2.15}$$

with

$$A(z, t=0) = 1, \quad \Gamma(z, t=0) = 1, \quad w(z, t=0) = 0,$$

and with periodicity of the solutions assumed on $[-\frac{1}{2}L, \frac{1}{2}L]$. Spatial derivatives are calculated by discrete Fourier transforms, and integration forward in time is accomplished by a fourth-order Adams–Moulton method. For these initial conditions, the two centroids are closest together at $z = 0$, and for $z \ll 1$, we have

$$\delta \approx 2 + z^2, \tag{2.16}$$

which is the initial condition considered by Saffman in his study. Such initial conditions correspond to two tubes with no initial axial flows, but with a pressure

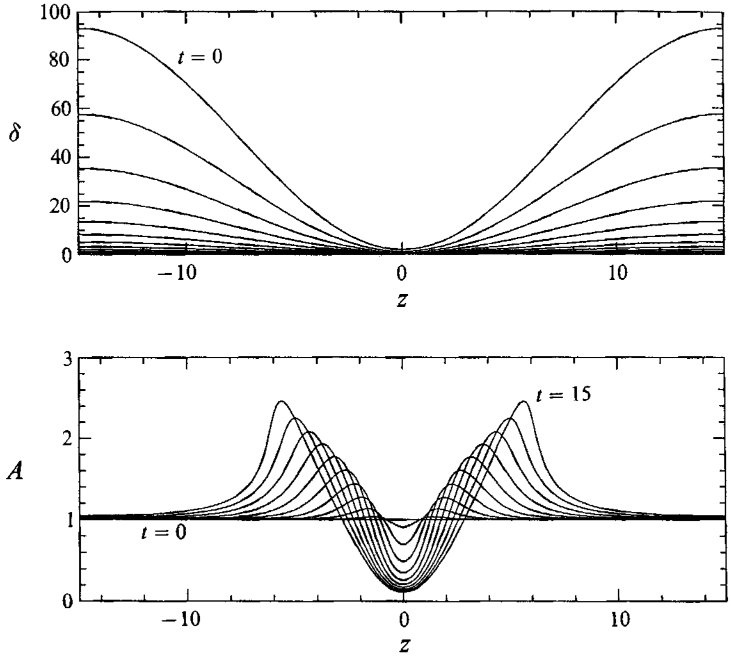

FIGURE 2. Numerical solution of the Saffman model. Plotted here are the separation δ and area A as a function of z for various times. The time ranges from 0 to 15 in steps of 1.5.

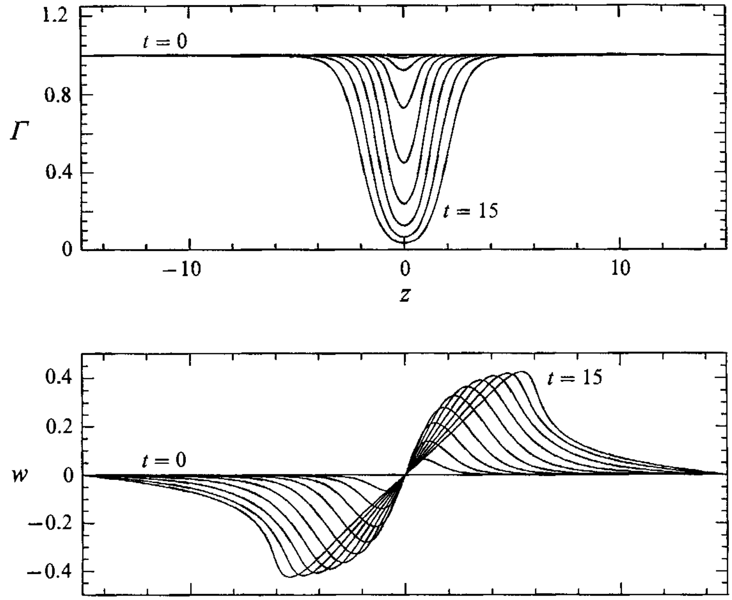

FIGURE 3. Numerical solution of the Saffman model. Plotted here are the circulation Γ and axial velocity w as a function of z for various times.

high in the plane of closest approach. In the numerical simulations, L is taken large enough so that the relevant results are independent of it. Figures 2 and 3 show the computed solutions to (2.11)–(2.14) with the above initial conditions. Here $\epsilon = 0.5$, $\mu = 10^{-3}$, and $L = 30$. The time t ranges from 0 to 15 in increments of 1.5. Figure 4

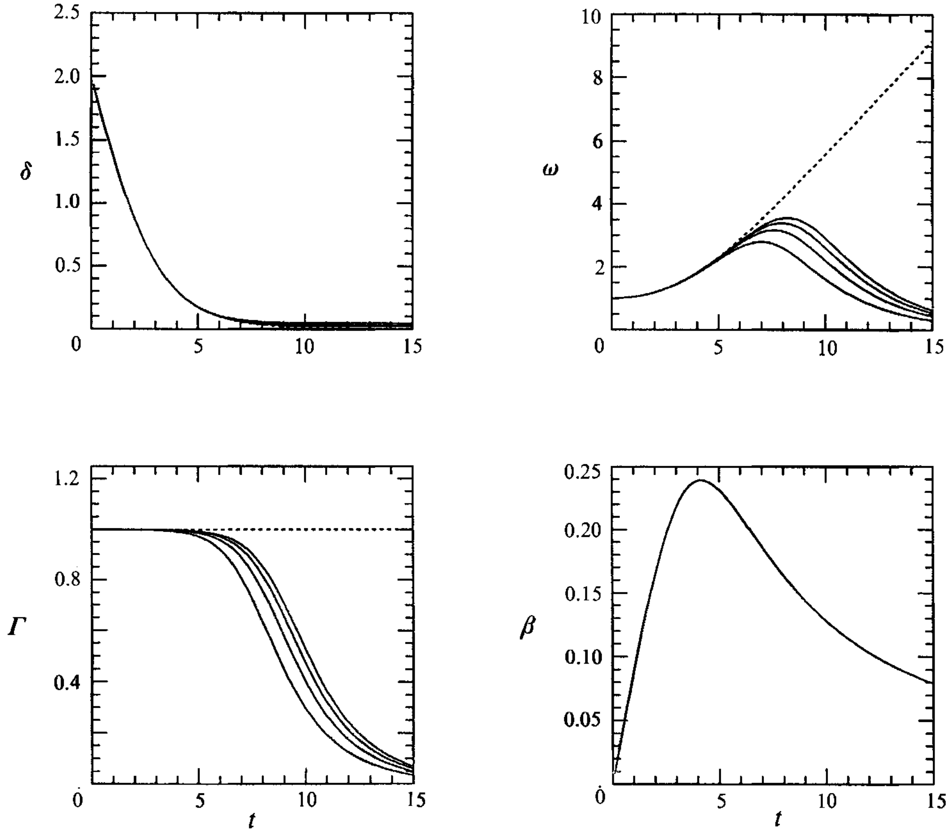

FIGURE 4. A plot of the separation δ, the vorticity ω, the circulation Γ, and axial rate of strain β as functions of time t at $z=0$ and at selected values of the inverse Reynolds number μ (see text). The inviscid limit $\mu=0$ is indicated by a dashed line.

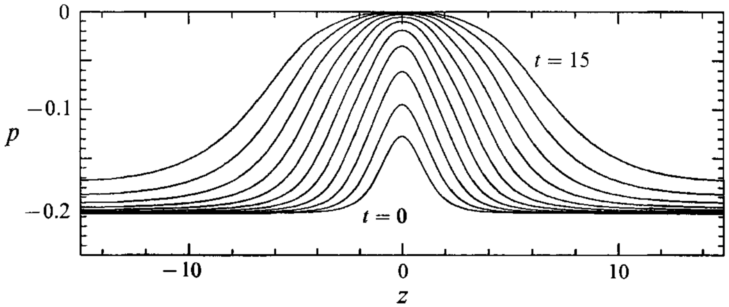

FIGURE 5. Variation of the pressure p with z at same times given in figure 2.

shows the separation, vorticity, circulation and axial rate of strain at $z=0$ as functions of time. The behaviour is typical of the model. Initially, the centroids collapse towards one another at $z=0$, driven by the straining flows. The axial out-of-plane strain rate β increases from zero, causing a decrease in the core area A. Provided that the centroid separation is greater than $O(\mu^{\frac{1}{2}})$, the circulation does not decay significantly and the vorticity ω increases rapidly through stretching. However, this process is not self-sustaining. As the centroids are driven together, the vortex cores become increasingly elongated and flattened. As the aspect ratio $\theta = h/b$ becomes large, the term $f(\theta)$ in the pressure, and thus the pressure itself, approaches

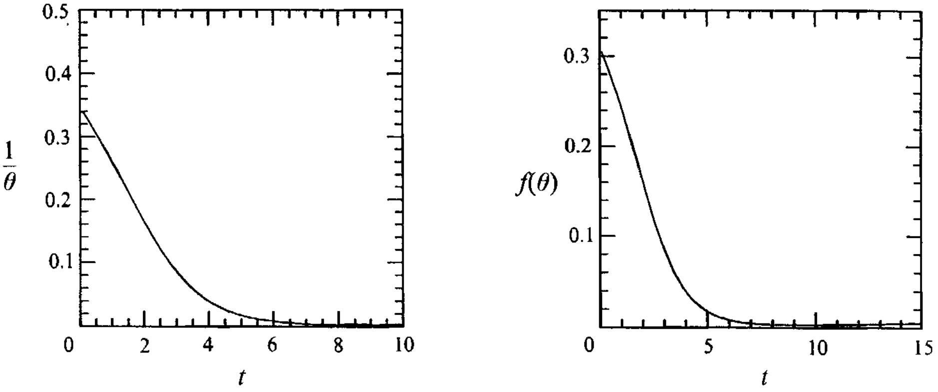

FIGURE 6. The functions $1/\theta$ and $f(\theta)$ at $z=0$ as functions of time.

zero. As the pressure is by definition here bounded from above by zero, this process leads to a broadening of the pressure distribution about $z=0$. Consequently, the pressure gradient is reduced, and a region of uniform pressure propagates outwards from the centre. Figure 5 shows the pressure (calculated from (2.14)) as a function of z at the same times as in figures 2 and 3. Figure 6 shows $1/\theta$ and $f(\theta)$ at $z=0$ as functions of time. This process does not stop until the centroids have reached the viscous lengthscale. Note that neither $1/\theta$ nor $f(\theta)$ go completely to zero. At this point, it is the decay of Γ, rather than $f(\theta)$, that drives the pressure p further towards uniformity in the reconnection region.

The decrease of β is a consequence of the diminution of the pressure gradient. At late times in the neighbourhood of $z=0$, we have demonstrated that

$$\partial^2 p/\partial z^2 \approx 0. \tag{2.17}$$

At such times the axial momentum equation (2.14) is now essentially the Burger's equation

$$\partial w/\partial t = -w\,\partial w/\partial z, \tag{2.18}$$

or

$$\frac{\partial}{\partial t}\left(\frac{\partial w}{\partial z}\right) = -\left(\frac{\partial w}{\partial z}\right)^2 - w\frac{\partial^2 w}{\partial z^2}. \tag{2.19}$$

Evaluating this expression at $z=0$, setting $\hat{\beta} = \partial w/\partial z|_{z=0}$, and noting that

$$\partial^2 w/\partial z^2|_{z=0} = 0$$

at all times from these initial conditions, we have

$$\mathrm{d}\hat{\beta}/\mathrm{d}t = -\hat{\beta}^2, \tag{2.20}$$

or

$$\hat{\beta} = C/(1+Ct). \tag{2.21}$$

This is precisely the behaviour observed in figure 4. We next examine the behaviour of the model as the effective viscosity μ is varied. Figure 4 shows the separation δ, the vorticity ω, the circulation Γ, and axial rate of strain β as functions of time t at $z=0$. The results are shown for $\mu = 1.0\times10^{-3}$, 0.5×10^{-3}, 0.33×10^{-3}, 0.25×10^{-3}, and $\mu=0$ (shown as a dashed curve).

There are several features worth noting:

(i) For large times, δ reduces to a value which is roughly $O(\mu^{\frac{1}{2}})$.

(ii) The location as a function of time of the peak vorticity increases with decreasing μ.

(iii) For $\mu=0$, the ultimate growth of the vorticity is only linear. This is due to the decay of the pressure gradient and the elongation of the vortex cores. The linear growth follows directly from the behaviour of $\hat{\beta}$ in (2.21).

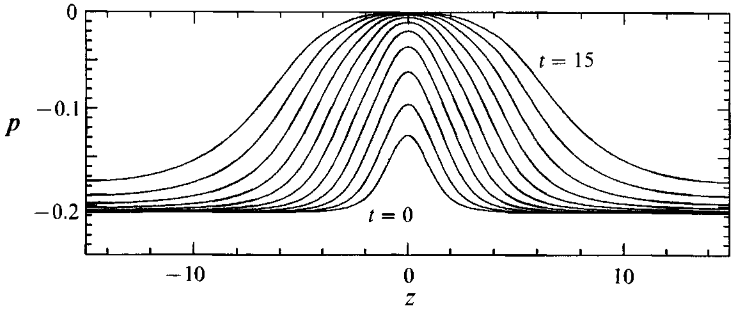

FIGURE 7. Behaviour of the pressure for $\mu = 0$.

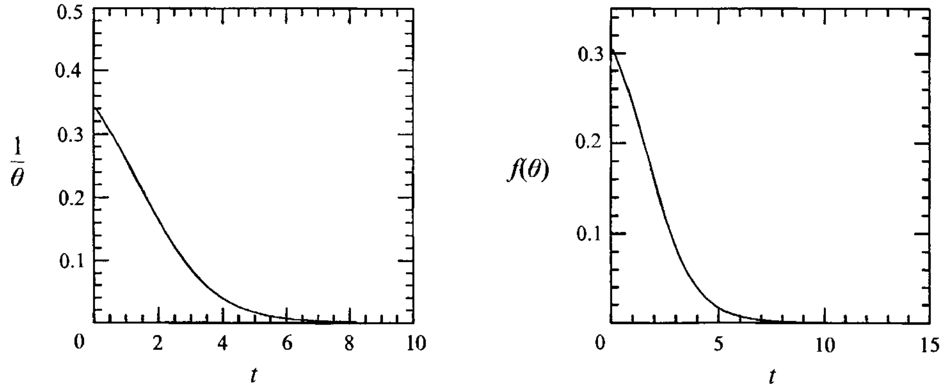

FIGURE 8. Plot of the functions $1/\theta$ and $f(\theta)$ *vs.* time for $\mu = 0$.

We define the reconnection time as the amount of time over which Γ decays to half of its initial value. The reconnection time increases with decreasing μ.

The strain rate β shows little dependence upon μ. This is because the process of decay of the pressure gradient proceeds on an essentially inviscid timescale. This is confirmed by calculations displayed in figures 7 and 8, which respectively show for $\mu = 0$ the pressure as a function of z, at the same times as in figure 4, and $1/\theta$ and $f(\theta)$, at $z = 0$ as functions of time. Note now that $1/\theta$ goes asymptotically to zero.

2.3. *Analytical solution at late times*

It is now straightforward to discuss the large-time behaviour of the Saffman model in the reconnection region, for which the numerical results presented above suggest that we should assume that the pressure gradient has disappeared, and seek special solutions to (2.11)–(2.14) of the form

$$\delta(z,t) = \hat{\delta}(t), \quad A(z,t) = \hat{A}(t), \quad \Gamma(z,t) = \hat{\Gamma}(t), \quad w(z,t) = \hat{\beta}(t)\, z.$$

By substituting this Ansatz into the equations of motion, these solutions can be found essentially in closed form as

$$\hat{\beta}(t) = \frac{\beta_0}{1+\beta_0 t}, \tag{2.22}$$

$$\hat{A}(t) = \frac{A_0}{1+\beta_0 t} + \mu \frac{t}{2}\left(\frac{2+\beta_0 t}{1+\beta_0 t}\right), \tag{2.23}$$

$$\hat{\Gamma}(t) = \Gamma_0 \exp\left(-\mu \int_0^t \frac{1}{\hat{\delta}^2(s)}\,\mathrm{d}s\right), \tag{2.24}$$

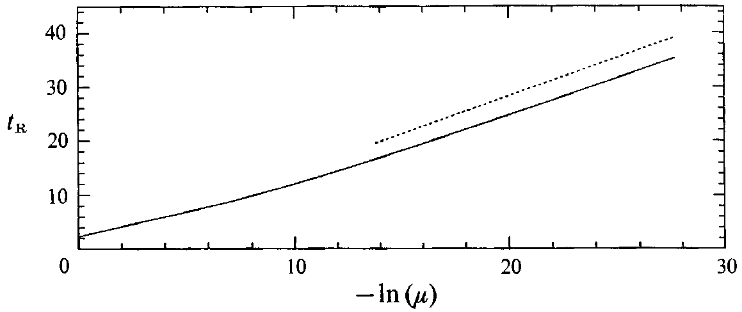

FIGURE 9. A plot of the reconnection time t_R (see text) *vs.* inverse Reynolds number μ (solid line). The asymptotic result of (2.31) is plotted for comparison (dashed line).

and

$$\hat{\delta}^2(t) = \delta_0^2 \frac{\exp(-2\epsilon^{\frac{3}{2}}t)}{(1+\beta_0 t)^2} + \mu\left[-\frac{\exp(-2\epsilon^{\frac{3}{2}}t)}{\epsilon^{\frac{3}{2}}(1+\beta_0 t)^2}\left(1-\frac{\beta_0}{\epsilon^{\frac{3}{2}}}+\frac{\beta_0^2}{2\epsilon^3}\right) + \frac{1}{\epsilon^{\frac{3}{2}}(1+\beta_0 t)^2}\left((1+\beta_0 t)^2 - \frac{\beta_0}{\epsilon^{\frac{3}{2}}}(1+\beta_0 t)+\frac{\beta_0^2}{2\epsilon^3}\right)\right]. \quad (2.25)$$

Here we make several further comments. Our numerics indicates that the solutions to the full set of equations (2.11)–(2.14) are attracted to these similarity solutions in a time only weakly dependent upon the viscosity μ. For fixed $\mu > 0$, as $t \to \infty$, we have

$$\hat{\beta} \to 0, \quad \hat{A} \to \infty, \quad \hat{\delta}^2 \to \mu/\epsilon^{\frac{3}{2}}, \quad \text{and} \quad \hat{\Gamma} \to 0.$$

The only quantity which might appear to deviate from the behaviour given above is the area A. Figure 2 shows no growth of A at $z = 0$. However, note that from (2.23) A increases to be $O(1)$ only on the very long timescale $O(1/\mu)$. If $\mu = 0$, we then have the special solutions

$$\hat{\beta}(t) = \beta_0/(1+\beta_0 t), \quad (2.26)$$

$$\hat{A}(t) = A_0/(1+\beta_0 t), \quad (2.27)$$

$$\hat{\delta}^2(t) = \delta_0^2 \exp(-2\epsilon^{\frac{3}{2}}t)/[(1+\beta_0)^2 t], \quad (2.28)$$

$$\hat{\Gamma}(t) = \Gamma_0. \quad (2.29)$$

Note that for these special inviscid solutions

$$\hat{\omega} = \hat{\Gamma}/\hat{A} = (\Gamma_0/A_0)(1+\beta_0 t). \quad (2.30)$$

That is, the vorticity grows only linearly, as observed in figure 4.

From the special solutions (2.22)–(2.25) it is now easy to extract the timescale for reconnection, as predicted by Saffman's model. Defining t_R by $\hat{\Gamma}(t_R) = \frac{1}{2}\Gamma_0$, substituting (2.24) into (2.25), we find that as $\mu \to 0$,

$$t_R \sim \ln(Re)/(2\epsilon^{\frac{3}{2}}) = \ln(1/\mu)/2\epsilon^{\frac{3}{2}}. \quad (2.31)$$

Recall however that we have scaled the time variable. In terms of dimensional time,

$$t_R^* = \ln(Re)/(2\alpha). \quad (2.32)$$

At long times this is the same timescale as that given by Kambe and Buntine & Pullin. We verify (2.31) in figure 9 by comparing the predicted reconnection time t_R with that calculated directly from numerical simulation of the Saffman equations.

The Saffman model does not include the effects arising from the translation and subsequent stretching of the vortices due to mutual induction. For this reason, it cannot be viewed as a valid description of the early-time behaviour of the tubes. There is evidence, however, from the results of Pumir & Siggia (1990) and the numerical results to be presented below, that the translational motion in the region of closest approach of the vortices eventually decreases substantially. At this point further stretching would be induced through the action of axial flows in and near the core. Because the straining flows at this point are, for the most part, externally imposed by the rest of the vortex, it is in this configuration that one might expect the Saffman model to provide physically consistent results. However, as we shall show below, the simple picture of the straining flow used in the Saffman model is not in accord with the results of numerical simulations. Thus, this aspect of the model would have to be improved upon in order to make quantitative comparisons.

3. Numerical solution of the Navier–Stokes equations

In order to assess the effect of core deformation on the dynamics generated by the close approach of two counter-rotating vortices, and to test the validity of the Saffman model we have performed numerical simulations of their interaction. The simulations described below are performed using two different numerical methods, both based upon pseudo-spectral techniques. For simplicity, we have chosen to examine the interactions in a triply periodic geometry. For moderate Reynolds numbers (up to 1500), a spectral method over a uniform grid is used. At higher Reynolds numbers, the range of scales generated by the flow cannot be adequately resolved by this method given the memory limitations of current supercomputers. Thus, an adaptive spectral method is employed which locally resolves the active region of the flow, at the expense of lower resolution for the remainder. The standard spectral method has an operation count of $O(N^3 \ln N)$ per time step, while the variable mesh method requires $O(N^4)$ operations per time step.

3.1. *Numerical implementation*

The equations of motion for the velocity $\boldsymbol{v}(x,y,z,t) = u\boldsymbol{i}+v\boldsymbol{j}+w\boldsymbol{k}$ and the dynamic pressure $P(x,y,z,t) = p+\frac{1}{2}\boldsymbol{v}\cdot\boldsymbol{v}$, for a given viscosity ν and unit density are the Navier–Stokes equations in rotation form:

$$\frac{\partial \boldsymbol{v}}{\partial t} = \boldsymbol{v}\times\boldsymbol{\omega}-\nabla P+\nu\nabla^2\boldsymbol{v}, \tag{3.1}$$

$$\nabla\cdot\boldsymbol{v} = 0, \tag{3.2}$$

where

$$\boldsymbol{\omega} = \omega_1\boldsymbol{i}+\omega_2\boldsymbol{j}+\omega_3\boldsymbol{k} \tag{3.3}$$

is the vorticity. The pressure can be related to the nonlinear term by computing the divergence of both sides of (3.1), and applying (3.2) to yield the Poisson equation

$$\nabla^2 P = \nabla\cdot(\boldsymbol{v}\times\boldsymbol{\omega}). \tag{3.4}$$

Since the geometry is periodic, it is possible to compute the pressure directly.

3.1.1. *Numerical integration in time*

The time-stepping algorithm for both fixed and variable mesh simulations consists of leap-frog differencing on the nonlinear term and pressure, which are related through (3.4), and Crank–Nicholson differencing on the diffusion term. This gives

$$(1-\nu\Delta t\,\nabla^2)\,\boldsymbol{v}^{(n+1)} = 2\Delta t(\boldsymbol{v}^{(n)}\times\boldsymbol{\omega}^{(n)}-\nabla P^{(n)})+(1+\nu\Delta t\,\nabla^2)\,\boldsymbol{v}^{(n-1)}, \tag{3.5}$$

$$\nabla^2 P^{(n)} = \nabla\cdot(\boldsymbol{v}^{(n)}\times\boldsymbol{\omega}^{(n)}), \tag{3.6}$$

where $\boldsymbol{v}^{(n)}, \boldsymbol{\omega}^{(n)}$ represent the value of the velocity and vorticity respectively at $t = n\Delta t$. This time integration method is second-order accurate. The main difference between the two numerical methods used in this work lies in the inversion of the elliptic equations for $\boldsymbol{v}^{(n)}$ and $P^{(n)}$.

3.1.2. *Spectral method utilizing a uniform grid*

The spectral method utilizing uniform grids is well established as a technique for accurately updating (3.5) and (3.6), and only an abbreviated discussion is given here (for example, see Canuto *et al.* 1988 or Gottlieb & Orszag 1977). Given the periodicity of the solution on the cube $[0, 2\pi]^3$, the solution is discretized over a uniform grid of $N_x \times N_y \times N_z$ points, in the x-, y-, and z-directions, respectively. The discrete solution may then be represented as a discrete Fourier series, which can be evaluated rapidly using the FFT algorithm. The nonlinear term is evaluated on the physical space mesh, where $\boldsymbol{\omega}$ is approximated from its discrete series representation. The Laplacian is diagonalized in this case by the discrete Fourier transform, and thus (3.6) is easily solved for the pressure. The diagonalization of the Laplacian allows the direct solution of $\boldsymbol{v}^{(n+1)}$ in (3.5). The advantage of the spectral method is that the spatial consistency error, for infinitely differentiable velocity and pressure fields, is of infinite order.

3.1.3. *Spectral method utilizing a stretched grid*

For the second spectral method, a periodic change of variable is introduced independently in each spatial variable x_i as

$$x_i = f_i(\xi_i), \quad i = 1, 2, 3. \tag{3.7}$$

Each $f_i(\xi_i)$ is a prescribed, infinitely differentiable function satisfying $f_i(0) = 0$ and $f_i(2\pi) = 2\pi$, with $f_i'(\xi_i)$ strictly positive and periodic on $[0, 2\pi]$. Derivatives with respect to x_i are replaced by

$$\frac{\partial}{\partial x} = \frac{1}{f_i'(\xi_i)}\frac{\partial}{\partial \xi_i} = q_i(\xi_i)\frac{\partial}{\partial \xi_i}. \tag{3.8}$$

The solution is now sampled at uniformly spaced values of ξ_i. This allows the discrete solution to be represented as a discrete Fourier transform, now in the new variables, and to again use this representation to approximate derivatives. As in the spectral method described previously, nonlinearities are evaluated in physical space. However, unlike the first method, the discrete Laplacian in (3.5) and (3.6) is now no longer diagonalized by the discrete Fourier transform, and different methods must be employed to solve these elliptic equations. Our approach will be to construct eigenfunctions which will diagonalize the discrete Laplacian.

As the change of variable is introduced independently in each variable, the elliptic equations remain separable. To construct these eigenfunctions, we need only solve, in each direction, the one-dimensional Sturm–Liouville problem

$$q(\xi)\frac{\partial}{\partial \xi}q(\xi)\frac{\partial}{\partial \xi}\psi_j = \mu_j \psi_j, \quad j = 0, 1, 2, \ldots, \tag{3.9}$$

with $\psi_j(\xi)$ periodic on the interval $[0, 2\pi]$. We represent these eigenfunctions as a superposition of Fourier modes in ξ. Using equally spaced values of ξ_i as our collocation points, (3.9) becomes

$$\boldsymbol{QDQD}\boldsymbol{\Psi}_j = \hat{\mu}_j \boldsymbol{\Psi}_j, \quad j = 0, \ldots, N-1. \tag{3.10}$$

Here periodicity implies that $\Psi_{j,0} = \Psi_{j,N}$. $\boldsymbol{Q}$ is an $N \times N$ diagonal matrix with strictly positive entries $[\boldsymbol{Q}]_{kk} = q(k\Delta\xi)$, and $\boldsymbol{D}$ is an $N \times N$ circulant and skew-symmetric difference operator of rank $N-2$, arising from the derivative approximation given by the discrete Fourier transform.

The eigenfunctions of (3.9) are of course $\cos(jf(\xi))$ and $\sin(jf(\xi))$, with $\mu_j = -j^2$. When $h(\xi) \equiv 1$ (giving $\boldsymbol{Q} = \boldsymbol{I}$), the eigenvectors of the discrete system (3.10) are $\psi_{j,k} = \cos(jk\Delta\xi)$ and $\sin(jk\Delta\xi)$, or the eigenfunctions of (3.9) evaluated at the collocation points $k\Delta\xi$, with eigenvalues $\hat{\mu}_j = \mu_j = -j^2$.

This is not generally the case for non-constant q because of the approximation made by discretizing ξ, and it is necessary to solve numerically for the discrete eigenvectors and eigenvalues of (3.10). This is done by diagonalization of the matrix $\boldsymbol{A} = \boldsymbol{QDQD}$ to give $\boldsymbol{A} = \boldsymbol{P}\Delta\boldsymbol{P}^{-1}$, where Δ is diagonal with $[\Delta]_{kk} = \hat{\mu}_k$. The matrix $\boldsymbol{A}$ has $\frac{1}{2}N$ distinct eigenvalues, each of multiplicity two, and while $\boldsymbol{A}$ is not symmetric, it is straightforward to show that its eigenvalues are real and non-positive. They are ordered so that $\hat{\mu}_0 = \hat{\mu}_1 = 0$, $\hat{\mu}_{2k} = \hat{\mu}_{2k+1}$ and $\hat{\mu}_{2k+1} \geqslant \hat{\mu}_{2k+2}$. The eigenvectors of $\boldsymbol{A}$ then give a basis for the discrete solution in that direction. In this basis, the representation of the solution is found by multiplication by $\boldsymbol{P}^{-1}$. This multiplication also yields the components of the solution associated with the zero eigenvalues; these are set to zero. Thus, the solution of each discrete elliptic equation requires two $N \times N$ matrix multiplications (by $\boldsymbol{P}^{-1}$ and $\boldsymbol{P}$), applied separately in three directions, against N^2 N-vectors. The operation count is thus $O(N^4)$. The matrix multiplication can be implemented very efficiently on vector processors as N^2 applications of, for example, the LINPACK routine SAXPY over vectors of length N^2. The specification of the actual stretching functions which are employed is deferred to the next section where we provide details of the initial conditions.

3.2. *Initial conditions and symmetries*

3.2.1. *Initial conditions*

The initial conditions used here are three-dimensional perturbations of two parallel circular vortices in close proximity to one another. The configuration of the initial vorticity field consists of two counter-rotating tubes of vorticity on either side of the plane $y = \pi$. The centroid of each tube is perturbed sinusoidally. The vorticity within a single unperturbed tube is axisymmetric about its centre and has a component in only the z-direction. That is, for an unperturbed vortex, setting the centroid at $x = y = 0$, we have

$$\boldsymbol{\omega} = \hat{\omega}(r)\boldsymbol{k} \quad \text{with} \quad r^2 = x^2 + y^2. \tag{3.11}$$

In this study, we have used the compact, infinitely differentiable vorticity distribution first employed by Melander, McWilliams & Zabusky (1987) and given by

$$\hat{\omega}(r) = \begin{cases} -20[1 - f(\frac{3}{2}r)] & \text{if} \quad r < \frac{2}{3}, \\ 0 & \text{if} \quad r \geqslant \frac{2}{3}, \end{cases} \tag{3.12}$$

with $$f(\eta) = \exp[-K \exp(\eta - 1)/\eta], \quad K = \tfrac{1}{2}\exp(2)\ln(2).$$

The initial condition considered here is given by

$$\hat{\boldsymbol{\omega}}(x, y, z) = [\hat{\omega}_3(\boldsymbol{r} - \boldsymbol{r}_+(z)) - \hat{\omega}_3(\boldsymbol{r} - \boldsymbol{r}_-(z))]\boldsymbol{k}, \tag{3.13}$$

where $$\boldsymbol{r}_+ = [\pi - \epsilon(1 - \cos z)\sin(\tfrac{1}{3}\pi)]\boldsymbol{i} + [\pi + b - \epsilon(1 - \cos z)\cos(\tfrac{1}{3}\pi)]\boldsymbol{j},$$

$$\boldsymbol{r}_- = [\pi - \epsilon(1 - \cos z)\sin(\tfrac{1}{3}\pi)]\boldsymbol{i} + [\pi - b + \epsilon(1 - \cos z)\cos(\tfrac{1}{3}\pi)]\boldsymbol{j},$$

where $2b$ is the spacing between the vortex centroids in the plane of closest approach. Following Melander & Hussain (1988, p. 257), we choose $2b = 1.73$.

After perturbing the vortices in this fashion, $\hat{\boldsymbol{\omega}}$ is not divergence free. We therefore project $\hat{\boldsymbol{\omega}}$ onto a divergence-free field by defining the initial velocity as

$$\boldsymbol{v}(x,y,z,t=0) = \boldsymbol{\nabla} \times (\nabla^2)^{-1}\hat{\boldsymbol{\omega}}, \tag{3.14}$$

and finally, the true initial vorticity field as

$$\boldsymbol{\omega}(x,y,z,t=0) = \boldsymbol{\nabla} \times \boldsymbol{v}(x,y,z,t=0). \tag{3.15}$$

While the projection yields a velocity with no component in the z-direction, it does introduce slight perturbations in the variation of the vorticity components with x and y. Note that the centroids of the two vortices are furthest apart in the plane $z=0$, and closest in the plane $z=\pi$. The plane $z=\pi$ will be referred to as the plane of closest approach. This plane is a material (free-slip) surface for the flow, and we have $\boldsymbol{v}|_{z=\pi} = u(x,y,\pi)\,\boldsymbol{i} + v(x,y,\pi)\boldsymbol{j}$, and $\boldsymbol{\omega}|_{z=\pi} = \omega_3(x,y,\pi)\,\boldsymbol{k}$.

Finally, we define the Reynolds number by

$$Re = \Gamma/\nu, \tag{3.16}$$

where Γ is the circulation in a cross-section of a single, unperturbed vortex core.

3.2.2. *Symmetries*

The set of initial conditions considered here have symmetries that are preserved by the equations of motion. These symmetries are exploited in the simulations to reduce the computational domain from $[0,2\pi]^3$ to $[0,2\pi]\times[0,\pi]\times[0,\pi]$. In particular, about $y=0$ and $y=\pi$, the velocities u and w are even functions of y while the velocity v is an odd function of y. Similarly, about $z=0$ and $z=\pi$, the velocities u and v are even functions of z while the velocity w is an odd function of z. As a consequence of these symmetries, the velocity and pressure fields will have the Fourier series representation

$$u(x,y,z,t) = \sum_{j=-\infty}^{+\infty} \sum_{k=0}^{+\infty} \sum_{l=0}^{+\infty} U_{jkl}(t)\,\mathrm{e}^{ijx} \cos ky \cos lz, \tag{3.17}$$

$$v(x,y,z,t) = \sum_{j=-\infty}^{+\infty} \sum_{k=1}^{+\infty} \sum_{l=0}^{+\infty} V_{jkl}(t)\,\mathrm{e}^{ijx} \sin ky \cos lz, \tag{3.18}$$

$$w(x,y,z,t) = \sum_{j=-\infty}^{+\infty} \sum_{k=0}^{+\infty} \sum_{l=1}^{+\infty} W_{jkl}(t)\,\mathrm{e}^{ijx} \cos ky \sin lz, \tag{3.19}$$

$$P(x,y,z,t) = \sum_{j=-\infty}^{+\infty} \sum_{k=0}^{+\infty} \sum_{l=0}^{+\infty} P_{jkl}(t)\,\mathrm{e}^{ijx} \cos ky \cos lz. \tag{3.20}$$

We note that in evaluating the velocity and pressure, half-range Fourier transforms may be employed in certain directions. We have made use of such transforms in both sets of simulations with a consequent reduction of computational work.

3.2.3. *Consequences of symmetry*

Four of the six faces of the computational volume $V = [0,2\pi]\times[0,\pi]\times[0,\pi]$ are free-slip surfaces of the flow. We merely exclude the periodic end faces $x=0$ and 2π. We label these four remaining faces Π (at $z=\pi$), Π' (at $y=\pi$), S (at $z=0$), and S' (at $y=0$) (see figure 1). Π is the horizontal face in the plane of closest approach, Π' is the vertical face separating the two oppositely signed vortices; S is the horizontal face where the two vortices are furthest apart; and S' is the vertical face whose presence is necessary due to the assumed periodicity of the flow. In the absence of viscosity, the circulation in each of these faces is a conserved quantity. In particular,

$$C_\Pi = \int_\Pi \omega_3 \,\mathrm{d}A \tag{3.21}$$

is conserved in the absence of dissipation. This is the quantity we expect to decay rapidly in our viscous calculations. There is also a kinematical balance among these four circulations which is valid even in the presence of viscosity. Using that $\nabla \cdot \boldsymbol{\omega} = 0$, the divergence theorem, and periodicity in x, we have

$$0 = \int_V \nabla \cdot \boldsymbol{\omega} \,\mathrm{d}V' = \int_{\partial V} \boldsymbol{\omega} \cdot \boldsymbol{n} \,\mathrm{d}A' = (C_\Pi + C_{\Pi'}) + (C_S + C_{S'}), \tag{3.22}$$

where $\boldsymbol{n}$ is the outward-facing unit normal to the volume V. This relation will be used in the next section.

In the plane of closest approach, the vorticity transport equation reduces to an equation of evolution for the z-component of $\boldsymbol{\omega}$, and has a particularly simple form. It is

$$\frac{\partial \omega_3}{\partial t} + u\frac{\partial \omega_3}{\partial x} + v\frac{\partial \omega_3}{\partial y} = \omega_3 \frac{\partial w}{\partial z} + \nu \nabla^2 \omega_3. \tag{3.23}$$

The stretching term is reduced to only the single term $\omega_3 \partial w/\partial z$. Note that $\partial w/\partial z$ is a principal rate of strain, with its associated vector (the z-axis) orthogonal to the plane of closest approach. Thus, in this region the evolution of vorticity is determined by the vorticity times the out-of-plane or axial strain rate, and the diffusion of vorticity. Note that the diffusion term in (3.23) involves derivatives in the z-direction. Equation (3.23) gives a very simple equation for the evolution of the vorticity at a critical point. Let $(X(t), Y(t))$ denote the path of a critical point in the plane of closest approach, i.e.

$$\partial \omega_3/\partial x|_{(X(t),\, Y(t))} = 0 \tag{3.24}$$

$$\partial \omega_3/\partial y|_{(X(t),\, Y(t))} = 0. \tag{3.25}$$

Let $\hat{\omega}_\mathrm{C}(t) = \omega_3(X(t), Y(t), \pi, t)$. Taking a time derivative of $\hat{\omega}_\mathrm{C}(t)$ and applying (3.23) yields

$$(\mathrm{d}/\mathrm{d}t)\, \hat{\omega}_\mathrm{C}(t) = \hat{\omega}_\mathrm{C}(t)\, (\partial w/\partial z)\, (X(t), Y(t), \pi, t) + \nu \nabla^2 \omega(X(t), Y(t), \pi, t). \tag{3.26}$$

If, for example, in (3.26) with $\nu = 0$, the scaling $\partial w/\partial z \sim \omega_3$ developed, a blow-up of the vorticity as in the Siggia–Pumir model would occur.

Similar statements hold also within the other symmetry planes, but it is within the region of closest approach that the vorticity shows its greatest stretching, gradient production, and dissipation. Our choice of stretching functions, $f_i(x_i)$, also reflects this; in our calculations with stretched grids, resolution is enhanced about and within the plane of closest approach.

3.2.4. *Choice of stretching functions*

As will be clear from the results, the generation of small scales is mostly concentrated in the reconnection region, that is, about $z = \pi$ and $y = \pi$. Thus, we have chosen the very simple stretching functions

$$y(\xi_2) = \xi_2 - \alpha_y \sin(\xi_2 - \pi) \tag{3.27}$$

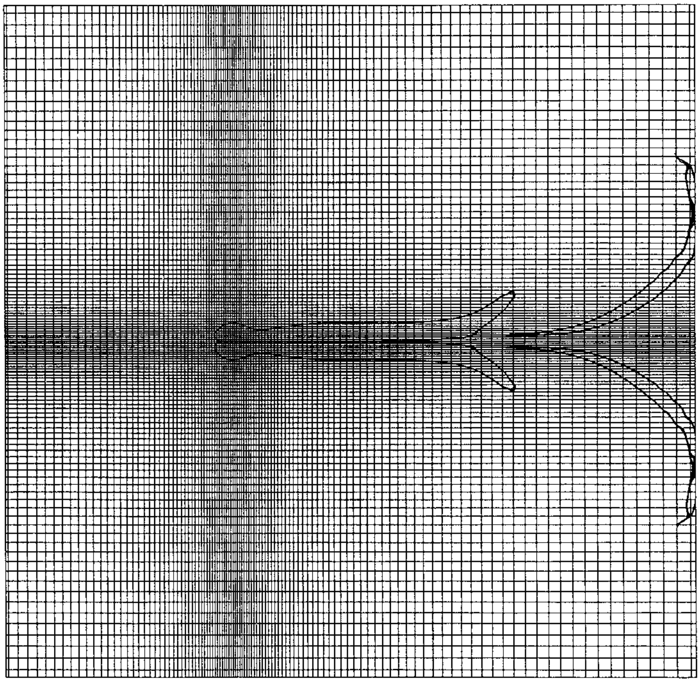

FIGURE 10. A plot of the stretched grid used to compute the flow, superimposed upon a contour at 4% of the maximum of the vertical vorticity ω_3 at $t = 1.50$.

$$z(\xi_3) = \xi_3 - \alpha_z \sin(\xi_3 - \pi). \tag{3.28}$$

This choice is equivalent to a local mesh size in the y-direction (for example) at $y = \pi$ of size $\Delta y = \Delta\xi_2(1-\alpha_y)$, where $\Delta\xi_2 = \pi/N_y$ and N_y is the number of points in the y-direction. Further, we introduce a change of variable in the x-direction:

$$x(\xi_1) = \xi_1 - \alpha_x \sin(\xi_1 - x_0), \tag{3.29}$$

where the choice of x_0 gives the most resolution in the x-direction at the point of maximum vorticity. This point is kept approximately fixed by the introduction of a time-dependent change of frame in the x-direction. This change of frame is found by performing a low-order polynomial fit to the path of the vorticity maximum from calculations at lower *Re*. For the highest Reynolds number calculations, this fit is refined so as to follow this path more closely, by refitting the path from previous calculations with a cubic spline. This gives some improvement in the results. In each calculation, the values of α_x, α_y, and α_z are time independent. Thus, the diagonalization of the elliptic operators, discussed in the previous section, need only be done at the beginning of the calculation. The implementation of the method was checked by comparison with the uniform grid results at lower *Re*, and early time results for higher *Re*. We also examined the effect of varying the values of α_x, α_y, and α_z. We found that in general the introduction of stretched meshes yielded more-resolved calculations, and allowed access to higher Reynolds numbers. For the results shown here, we have used $\alpha_x = \alpha_y = \alpha_z = \frac{3}{4}$. That is, the local resolution in the reconnection region is four times that of the uniform mesh method using the same number of points.

The calculations at $Re = 3500$ to be detailed below were performed using the variable-mesh method discussed above. From $t = 0$ to 1.1875 the resolution was

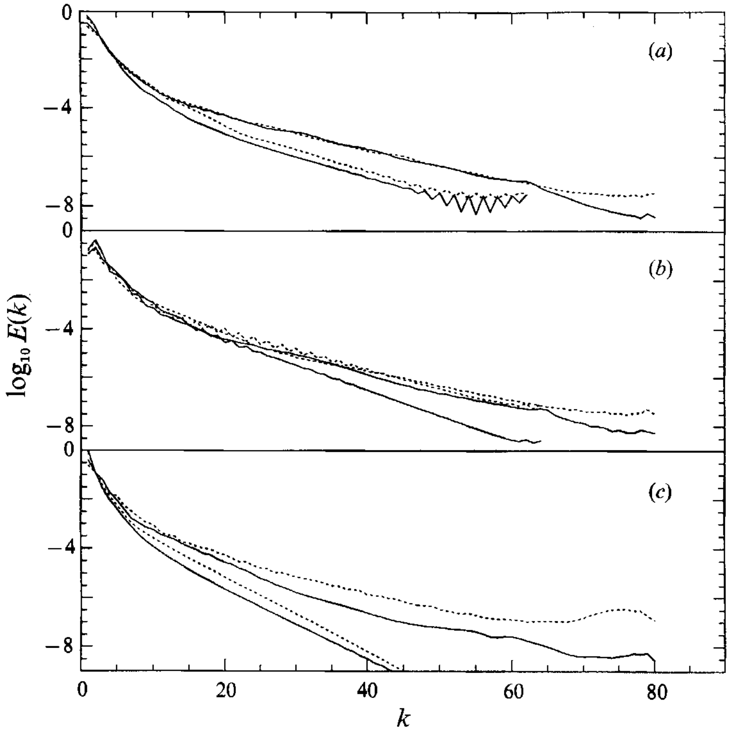

FIGURE 11. The directional spectra computed in the ξ_i variables, for Reynolds number 3500, at $t = 0.5$ (solid), 0.75 (dashed), 1.25 (solid), and 1.50 (dashed). The first two times are calculated from 128^3 data and terminate at $k = 64$, while the last two are from 160^3 data and terminate at $k = 80$. Shown here are spectra in (*a*) the x-direction, (*b*) the y-direction and (*c*) the z-direction.

$N_x = 128$ and $N_y = N_z = 64$ on the quarter-cube $[0, 2\pi] \times [0, \pi] \times [0, \pi]$, with the time-step $\Delta t = 0.00125$. At $t = 1.1875$ the resolution was increased to $N_x = 160$ and $N_y = N_z = 80$, and the time-step decreased to $\Delta t = 0.000625$.

3.2.5. *Resolution of the adaptive method*

In order to give some feeling for the resolution attained by our adaptive numerical method, figure 10 shows the grid used in the highest-resolution calculation (160^3 on the whole cube, disregarding symmetries). The grid is overlaid with the boundaries of the computed vortex cores in the plane of closest approach for a run to be discussed in detail below with $Re = 3500$ at $t = 1.50$. This is when the maximum vorticity is realized at that Reynolds number; the boundary is a vorticity contour at about 4% of the maximum. The grid is most dense about the region of maximum vorticity and provides there a local resolution equivalent to the use of 640 points in each direction.

3.2.6. *Directional spectra*

A further check on the accuracy of the results to be discussed below can be obtained from an examination of directional spectra. Figure 11 shows the associated directional spectra, computed in the ξ_i mapping variables (see (3.7)), at $t = 0.5$, 0.75, 1.25, and 1.50. The directional x-spectrum, for example, is defined by

$$E(k_1) = \sum_{k_2, k_3} |A_k|^2, \tag{3.30}$$

where A_k is the Fourier transform of v taken with respect to the ξ_i variables,

$$A_k = \int_{[0,\,2\pi]^3} v(x(\xi_1), y(\xi_2), z(\xi_3))\, \mathrm{e}^{\mathrm{i}k\cdot\xi}\, \mathrm{d}\xi. \tag{3.31}$$

It is in the (separable) mapping variables ξ_i that the numerically computed solution is represented and in which it should be well resolved. Aside from a trivial translation in the x-direction, these three mappings are fixed in time and have equal stretching factors. The first two times are calculated from 128^3 data, while the last two are from 160^3 data. Again, the decay of the spectra indicates that the calculations are well resolved, although we do note some accumulation of energy near the Nyquist frequency in the z-spectra at $t = 1.50$. This indicates that the z-direction is actually the hardest direction to resolve. This is somewhat surprising in that one would have expected the direction in which the vortices are most compressed (the y-direction) to be the most difficult to resolve. Apparently, the reconnection event generates high curvatures along the z-direction as well. This is consistent with the behaviour of the axial strain (see below); at later times we found the axial direction the most difficult to resolve. As this difficulty was lessened by increasing the grid stretching in the z-direction, it appears to arise from the local behaviour of the flow around $z = \pi$, rather than from the less-resolved outer flow.

We now turn to a detailed discussion of the numerical results.

3.3. *Numerical simulation of reconnection*

First, we will examine the evolution from the initial conditions given in (3.13) for $Re = 3500$. Subsequently, we will examine the effect of varying the Reynolds number. For these calculations we have taken $\epsilon = \frac{1}{2}$, which yields cores that abut each other slightly in the plane of closest approach.

3.3.1. *Volume rendering of the solution*

Figures 12(*a–e*) (plate 1) and 13(*a–e*) (plate 2) display the evolution of the vorticity fields at various times ($t = 0$, 0.75, 1.25, 1.50 and 1.75) during the reconnection process. To see the evolution and reconnection of the vortex tubes in the 'large', figure 12 shows volume renderings of the vorticity magnitude over two periods of the flow in the z-direction. Conversely, figure 13 shows volume renderings over a half-period in the z-direction, from a viewpoint which allows one to see down into the region of closest approach. The 'voxels' are coloured by the magnitude of the vorticity, with the most intense vorticity appearing as red. The relation of colour to vorticity magnitude is shown in the colour bar in figure 13, and is the same in each rendering. Note that the colour bar is heavily biased towards the higher levels of vorticity (shown in red), yet relatively little red appears in the figure. This is a manifestation of the large gradients of vorticity in the region of closest approach. While contour plots (see below) show clearly the large vorticity gradients, the volume of these regions is quite small and hence little red appears in the volume rendering. This small volume is further obscured by the voxels corresponding to lower magnitudes of vorticity despite the fact that we have made voxels corresponding to these lower levels partially transparent.

The figures display the global reconfiguration of the vorticity vector field through the breaking of vortex lines near the plane of closed approach. The rendering (figure 12*a*) at $t = 0$, shows the initial condition as a perturbation of two-dimensional flow, with the tubes in closest proximity in the region of the plane of closest approach $z = \pi$ (and $z = 3\pi$). The upper tube appears to be straight, but this is only apparent

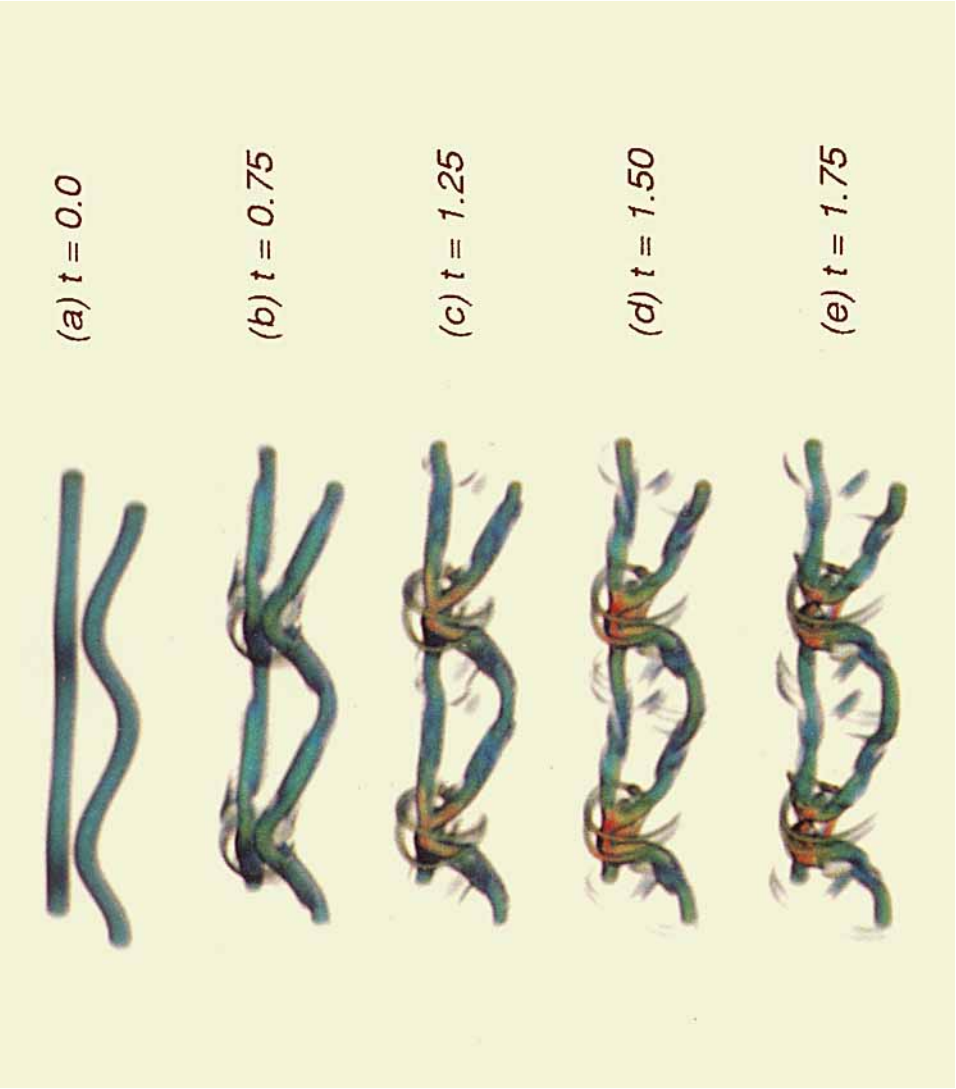

FIGURE 12. Volume rendering of vorticity magnitude for Re=3500 at *(a)* t=0, *(b)* 0.75, *(c)* 1.25, *(d)* 1.50, *(e)* 1.75. Two periods of the vortex tubes are shown here.

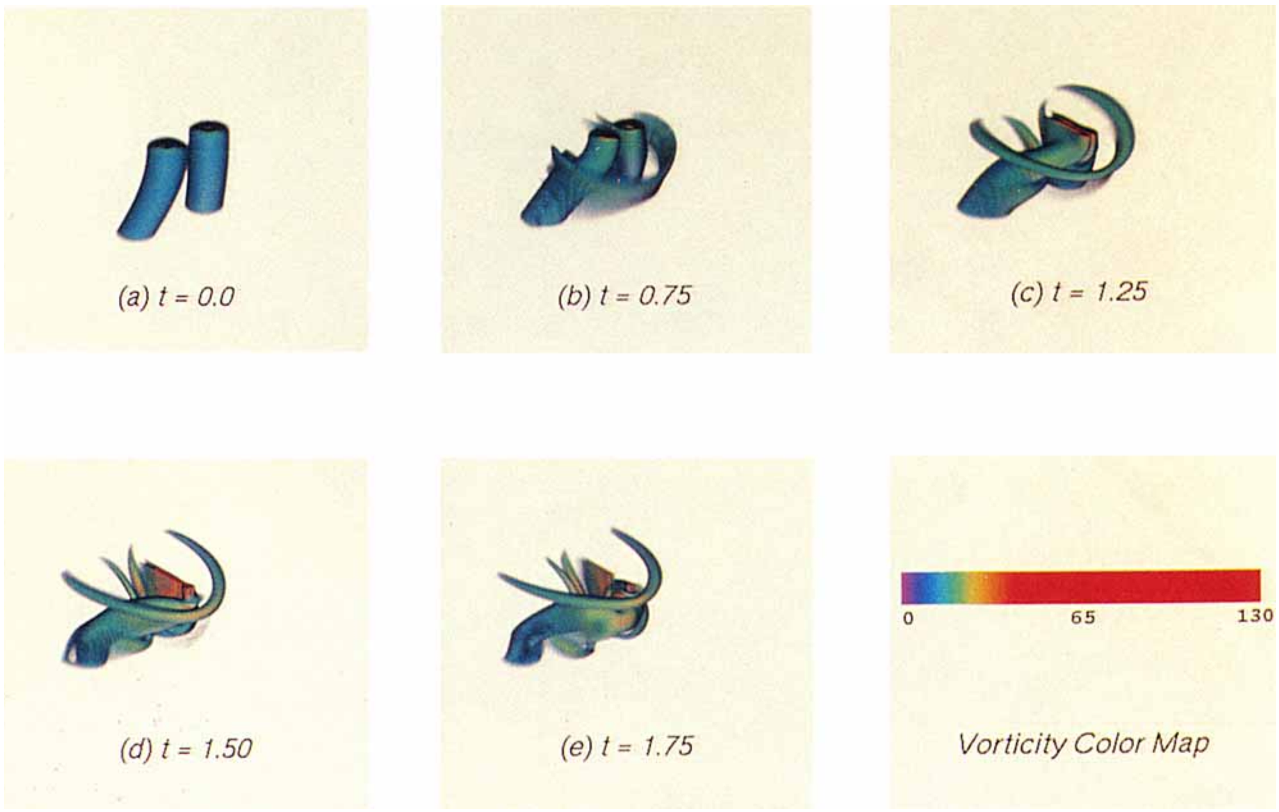

FIGURE 13. Volume rendering of vorticity magnitude for $Re=3500$ at *(a)* $t=0$, *(b)* 0.75, *(c)* 1.25, *(d)* 1.50, *(e)* 1.75. One-half of a period of the vortex tubes is shown here. The colour palette is also shown for both volume-rendering figures.

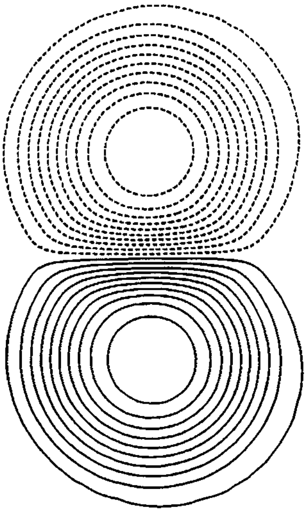

FIGURE 14. Initial conditions for a simulation at $Re = 3500$. Contours of ω_3 at $t = 0$. Here $x_{\min} = 0.78$, $x_{\max} = 3.92$, $c_{\min} = -20$, $c_{\max} = +20$, and $\Delta c = 2$, where $c_{\min}$ is the minimum value of a contour level, $c_{\max}$ the maximum value, and Δc is the contour level increment. The contour plots display the region $x_{\min} \leqslant x \leqslant x_{\max}$ and $\frac{1}{2}\pi \leqslant y \leqslant \frac{3}{2}\pi$. This notation will be used on subsequent contour plots. Note that all contour plots are of length π on a side.

in that its perturbation rises out of the viewing plane. Figure 13(*a*) again shows the two tubes, but truncated at $z = 0$ on the bottom, and at $z = \pi$ on the top. By $t = 0.75$ (figures 12*b* and 13*b*) the perturbation has grown because the tubes in the region of closest approach have a higher translational velocity relative to the remainder of the vortices. Significant axial flows have now developed, and it is from this time that the maximum vorticity, which lies in Π, becomes aligned with positive axial strain (see (3.23)) and begins to increase rapidly. At $t = 1.25$ (figures 12*c* and 13*c*), the vorticity is still increasing, but the tubes in the region of the maximum are also becoming increasingly flattened. This leads both to the rapid dissipation of vorticity there through viscous cancellation, and to a control on the rate of mutually induced stretching through a decrease in the translational velocity. At $t = 1.50$ (figures 12*d* and 13*d*), the vorticity has reached its maximum value in the calculation, its growth cut off by the dissipation of vorticity. This maximum again occurs in the plane of closest approach and is about seven times its initial value. The circulation of the vortex cores there has decayed to 70% of its initial value. Note that the two vortex tubes, above and below the plane of closest approach, have begun to orient themselves towards one another. From this time, the vorticity in Π decays very rapidly, virtually annihilating the vortex tubes there. This allows the vorticity field to reconfigure itself. By $t = 1.75$ (figures 12*e* and 13*e*) this process is complete, and leaves in its wake a series of vortex 'rings'. Note that vestigial amounts of vorticity remains, joining the rings. The circulation in the region of closest approach does not decay to zero. Plots of the vorticity vector field at this time do show that the vector field of the ring is now truly connected across the plane $y = \pi$, which initially separated the two vortices. We observe also the amplification of background vorticity near the tubes. This phenomenon was first noted by Melander & Zabusky (1989). Further, as the reconnection process proceeds, the development of helical disturbances in the vortex cores is observed.

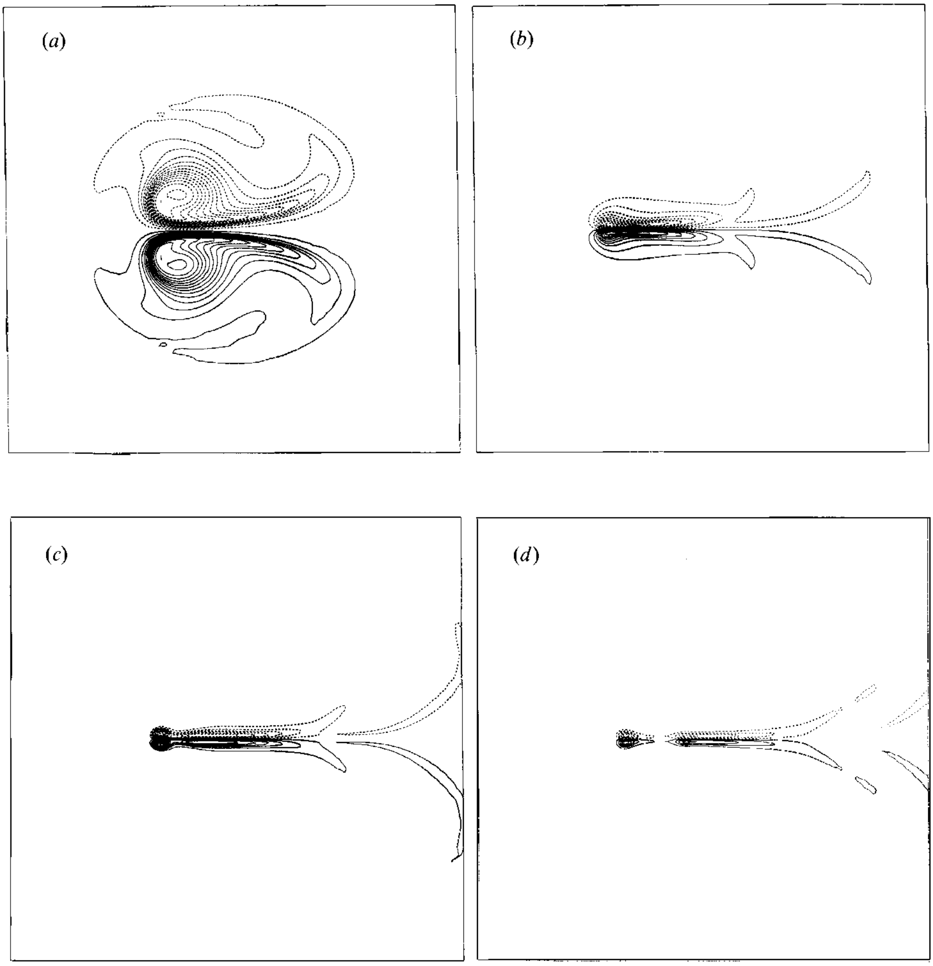

FIGURE 15. Contours of ω_3 for $Re = 3500$ at (*a*) $t = 0.75$ ($c_{\min} = -27$, $c_{\max} = +27$, $\Delta c = 2$), ($x_{\min} = -0.273$, $x_{\max} = 2.868$), (*b*) $t = 1.25$ ($c_{\min} = -85$, $c_{\max} = +85$, $\Delta c = 10$), ($x_{\min} = -1.052$, $x_{\max} = 2.089$), (*c*) $t = 1.50$ ($c_{\min} = -125$, $c_{\max} = +125$, $\Delta c = 10$), and ($x_{\min} = -1.328$, $x_{\max} = 1.813$), (*d*) $t = 1.75$ ($c_{\min} = -45$, $c_{\max} = +45$, $\Delta c = 10$) ($x_{\min} = -1.464$, $x_{\max} = 1.677$) (see figure 14 for notation).

3.3.2. *Core deformation*

We now focus our attention more closely on the interaction of the vortex tubes in the reconnection region. Of particular interest is the process of core deformation. The dynamics at $Re = 3500$ are illustrative of our calculations. Figure 14 shows the contours of ω_3 in the $z = \pi$ plane, at $t = 0$. Figures 15–17 show the contours of ω_3, $\partial w/\partial z$ and $\nu\nabla^2\omega_3$, respectively, in the $z = \pi$ plane, at $t = 0.75$, 1.25, 1.50, and 1.75. These times were chosen as they each illustrate a distinct portion of the reconnection process as observed in our calculations.

The vorticity does not begin to stretch immediately from $t = 0$. At $t = 0$, $\partial w/\partial z = 0$ everywhere, and for short times the maximum of ω_3 in Π actually lies in a region of slightly negative $\partial w/\partial z$. But by $t = 0.75$ (figure 15*a*), the vorticity maximum has become aligned with positive $\partial w/\partial z$ and begins to increase. Significant core deformation has already occurred as the two vortices have been flattened against one another. This deformation is not fore-and-aft symmetric, with the extrusion to the right of oppositely signed, elongated ribbons of vorticity. Referring to figure 16(*a*),

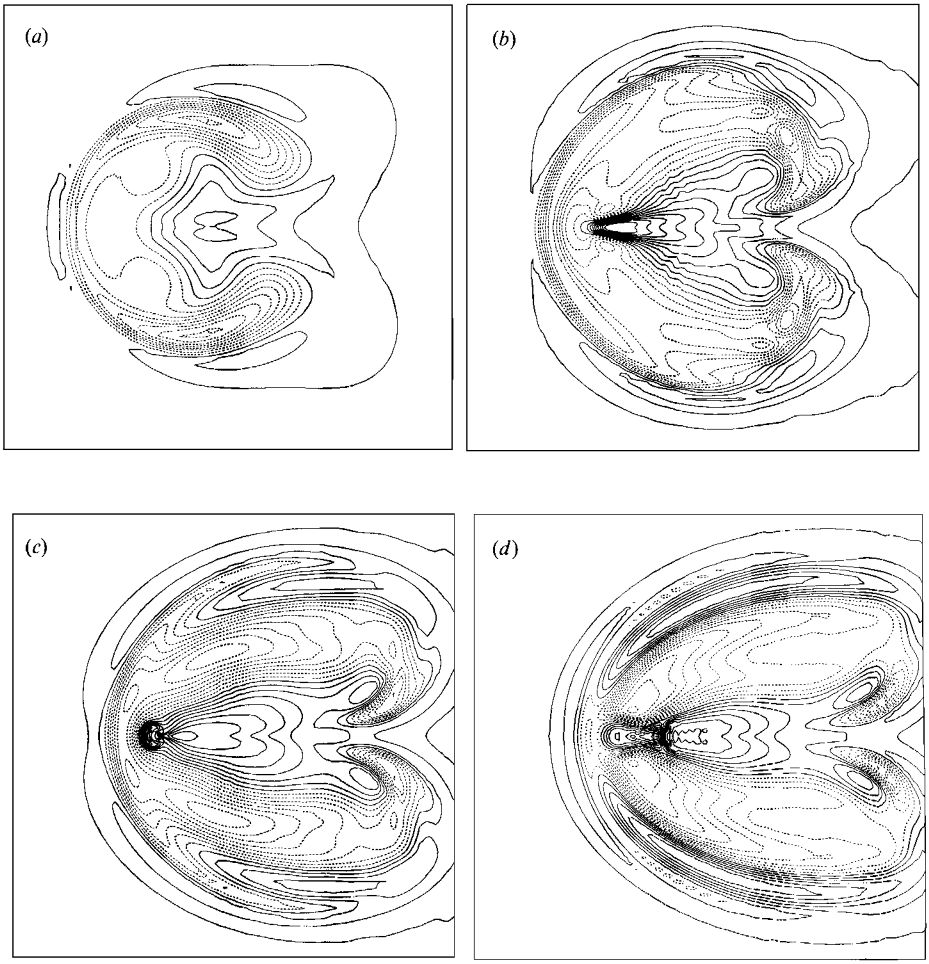

FIGURE 16. Contours of $\partial w/\partial z$ for $Re = 3500$ at (*a*) $t = 0.75$ ($c_{\min} = -6.5$, $c_{\max} = +3.5$, $\Delta c = 1$), ($x_{\min} = -0.273$, $x_{\max} = 2.868$), (*b*) $t = 1.25$ ($c_{\min} = -6.5$, $c_{\max} = +10.0$, $\Delta c = 1$), ($x_{\min} = -1.052$, $x_{\max} = 2.089$), (*c*) $t = 1.50$ ($c_{\min} = -8.5$, $c_{\max} = +8.5$, $\Delta c = 1$), and ($x_{\min} = -1.328$, $x_{\max} = 1.813$), (*d*) $t = 1.75$ ($c_{\min} = -9.5$, $c_{\max} = +8.5$, $\Delta c = 1$) ($x_{\min} = -1.464$, $x_{\max} = 1.677$) (see figure 14 for notation).

it is seen that these ribbons sit well within the region of positive axial strain $\partial w/\partial z$. Thus, the vorticity in the ribbons will be further enhanced and flattened. This behaviour is typical of our calculations and leads to the rapid dissipation of vorticity through viscous cancellation. In accordance with this point of view, figure 17(*a*) shows that strong dissipation is occurring along the extended ridge in ω_3 which runs the length of the vortex tails.

At $t = 1.25$ (figures 15*b*, 16*b*, and 17*b*), vorticity stretching is now well underway, as indicated by the reduced support of the two vortices in the plane of closest approach. The vorticity magnitude has now increased to four times its initial value. The vortices have an aspect ratio of about 7.5 : 1, and have become yet more flattened against each other. Again, the ribbons lie in the region of positive axial strain rate, and again it is along the ribbons that the greatest dissipation is taking place.

At $t = 1.5$ (figures 15*c*, 16*c*, and 17*c*), the vorticity has reached its maximum value in the calculation, which is about seven times its initial value. The diffusion term is

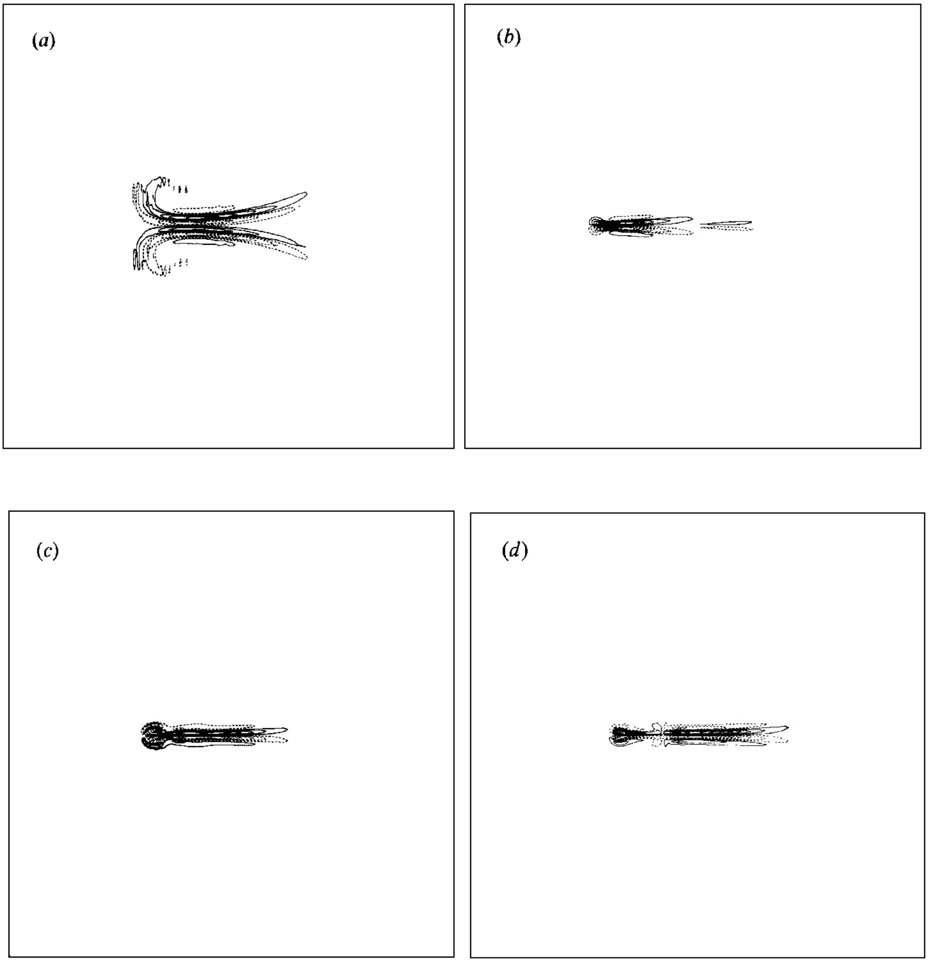

FIGURE 17. Contours of $\nu\nabla^2\omega_3$ for *Re* = 3500 at (*a*) $t = 0.75$ ($c_{\min} = -45$, $c_{\max} = +45$, $\Delta c = 10$), ($x_{\min} = -0.273$, $x_{\max} = 2.868$), (*b*) $t = 1.25$ ($c_{\min} = -850$, $c_{\max} = +850$, $\Delta c = 100$), ($x_{\min} = -1.052$, $x_{\max} = 2.089$), (*c*) $t = 1.50$ ($c_{\min} = -850$, $c_{\max} = +850$, $\Delta c = 100$), and ($x_{\min} = -1.328$, $x_{\max} = 1.813$), (*d*) $t = 1.75$ ($c_{\min} = -425$, $c_{\max} = +425$, $\Delta c = 50$) ($x_{\min} = -1.464$, $x_{\max} = 1.677$) (see figure 14 for notation).

now comparable to the stretching term, and it is from this time that the vorticity magnitude begins a rapid decay. In fact, the decay of the vorticity magnitude from this time is as rapid as was its increase through stretching. That is, the reduction of the vorticity crossing Π is occurring on a nearly convective timescale. The circulation in Π has decreased to 70% of its initial value. The vorticity distribution in Π has become yet more elongated and flattened, with each vortex now separated into a small, nearly circular vortex at the head, trailed by the ribbons. The aspect ratio of the vortices is about 17:1. The dissipation of vorticity is largest at the head.

By $t = 1.75$ (figures 15*d*, 16*d*, and 17*d*), the vorticity in Π is now strongly dissipated, and its maximum value has decreased to about a half of the value at $t = 1.50$. The circulation in Π is at 40% of its initial value. The global maximum of the vorticity now resides in the newly formed vortex ring, observed in figure 12(*d*), rather than in the plane of closest approach. The reconnection process is complete.

To study further the vortex core deformation, and in particular the formation of

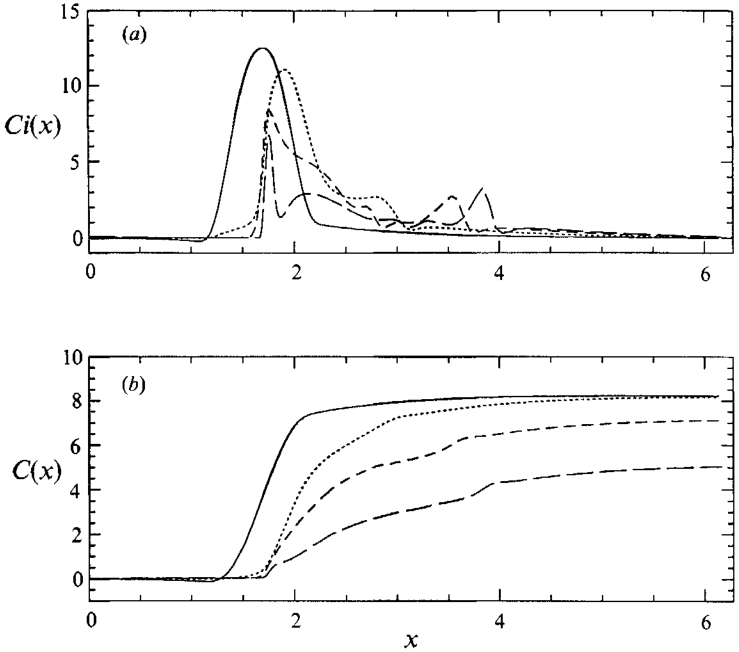

FIGURE 18. (*a*) The quantity $Ci(x)$ (see text) shown at times $t = 0$ (solid curve), 0.75 (short-dashed), 1.25 (medium-dashed), and 1.50 (long-dashed). (*b*) The circulation $C(x)$ (see text) shown at the same time as in (*a*).

the ribbons, we examine more closely the distribution of vorticity within the vortices. Figure 18(*a*) shows the integrated vorticity

$$Ci(x) = \int_0^{\pi} \omega_3(x, y, z = \pi)\,\mathrm{d}y.$$

That is, $Ci(x)$ measures the amount of vorticity along a vertical cut through the vortex, and the variations in $Ci(x)$ can be identified with specific features of the vortex. Figure 18(*b*) shows

$$C(x) = \int_0^{x} Ci(s)\,\mathrm{d}s,$$

at the same times. Thus $C(x)$ is the circulation in the rectangle $[0, x] \times [0, \pi]$ ($C(2\pi) = C_{\Pi}$), and measures the relative contributions that the structures in the vortex make to the circulation in Π.

At $t = 0$, the graph of $Ci(x)$ corresponds to the nearly symmetric vortex shown in figure 14. At $t = 0.75$, the appearance of the ribbons is reflected in $Ci(x)$ as the plateau to the right of the peak. While $C(2\pi)$ is hardly changed in its value from $t = 0$, approximately 30 % of the circulation now resides in the ribbons. This portion has increased to 67 % by $t = 1.25$, the circulation has begun to decay significantly, and the vorticity distribution is becoming increasingly non-uniform. At $t = 1.50$ while the head of the vortex has become well-separated from the ribbons, and while the vorticity maximum is located there, it contributes only 15 % of the total circulation.

3.3.3. *Reconnection and the decay of* C_{Π}

The rapid decay of C_{Π} can be related directly to the observed phenomenon of reconnection. Recall the kinematical relation $C_{\Pi} + C_{\Pi'} = -(C_S + C_{S'})$ (equation (3.22)), and that each circulation is conserved in the absence of viscosity. It is seen

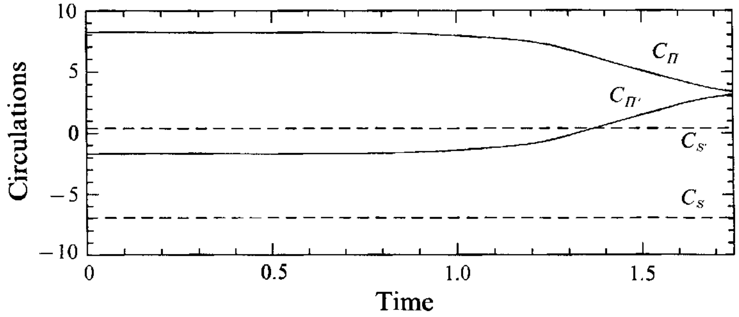

FIGURE 19. The four circulations, C_Π, $C_{\Pi'}$, C_S, and $C_{S'}$ shown as functions of time, for $Re = 3500$.

that the two free-slip faces S and S' remain well separated from the region of strong interaction between the two vortices. Thus, in the presence of viscosity, C_S and $C_{S'}$ should change only on a timescale that is long relative to the timescale of rapid decay in C_Π. Then, considering $C_S+C_{S'}$ to be a constant over this fast timescale, $C_\Pi+C_{\Pi'}$ is also a constant, and rapid decay of C_Π must give a likewise rapid increase in $C_{\Pi'}$. This is vortex reconnection; the presence of viscosity not only quickly reduces the amount of vorticity crossing Π, but also allows the augmentation of vorticity crossing Π'. It is precisely this behaviour that is manifested in our simulations. Figure 19 shows these four circulations as functions of time. Their behaviour indeed suggests the presence of well-separated timescales in this flow. Over the period of the calculation, C_S and $C_{S'}$ are nearly constant; individually and as a sum, they change in value by less than 1%. Conversely, C_Π shows rapid decay, and $C_{\Pi'}$ shows rapid increase (as it must) as vorticity becomes connected across the face Π' (the creation of positive circulation in Π' corresponds to vorticity connecting the two initially unconnected tubes). Melander & Hussain (1989) also observed the transfer of circulation from Π to Π' in their computations. The kinematic balance of circulation and the presence of well-separated timescales in this balance provide an explanation for this behaviour.

3.4. *Effect of varying Re and comparison with theory*

We next consider the effect of varying the Reynolds number in an attempt to deduce the infinite Reynolds number limit and to compare these results with the predictions of the Saffman model. Owing to accuracy and stability constraints, our numerical investigation is necessarily limited to moderate Reynolds numbers. Nevertheless, some informative behaviour is seen as the Reynolds number is increased.

3.4.1. *Variation of the maximum vorticity*

Figure 20(*a–d*) shows the contours of ω_3, at $t = 1.50$, in the plane of closest approach for the four largest Reynolds numbers, $Re = 2000$, 2500, 3000, and 3500. At $t = 1.5$ the calculation with $Re = 3500$ attains its greatest vorticity magnitude. In all these cases, the maximum vorticity occurs in the leading head of the vortex, and few obvious differences are observed in the spatial structure of the vorticity aside from the vortices being slightly flatter and more elongated at higher Reynolds numbers. Figure 21 shows $Ci(x)$ and $C(x)$ for the same Reynolds numbers. Examination of $Ci(x)$ shows that the structure of the vorticity in non-uniform, with the effect of increasing Reynolds number being the increasing separation of the head of the vortex from the trailing ribbons of vorticity. Very little dependence upon the Reynolds number is seen in $C(x)$.

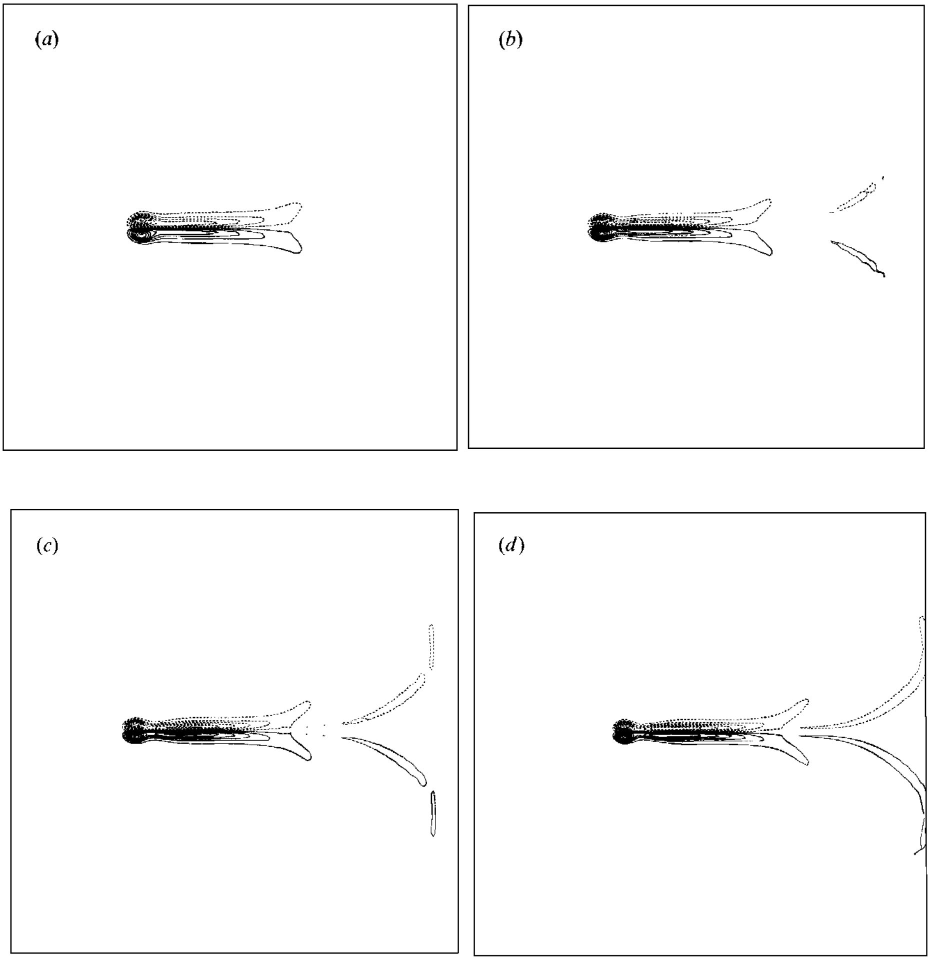

FIGURE 20. The contours of ω_3 in the $z = \pi$ plane for (*a*) $Re = 2000$ ($c_{\min} = -85$, $c_{\max} = +85$, $\Delta c = 10$), (*b*) $Re = 2500$ ($c_{\min} = -105$, $c_{\max} = +105$, $\Delta c = 10$), (*c*) $Re = 3000$ ($c_{\min} = -115$, $c_{\max} = +115$, $\Delta c = 10$), (*d*) $Re = 3500$ ($c_{\min} = -125$, $c_{\max} = +125$, $\Delta c = 10$), at $t = 1.50$.

Figure 22(*a*) shows the maximum of the vorticity in Π, i.e. ω_3, for the Reynolds numbers 1000, 1500, 2000, 2500, 3000 and 3500. This is also the global maximum of $|\omega|$ until the vorticity in Π has become more dissipated. Figure 22(*b*) shows the axial strain $\partial w/\partial z$ at the point of maximum vorticity in Π. In the absence of viscosity, it is $\partial w/\partial z$ at this point that determines the rate of growth of the maximum vorticity (see (3.26)), and it is the behaviour of the maximum vorticity alone that determines the smoothness of solutions to the Euler equations (Beale *et al.* 1984). We are thus particularly interested in the behaviour of these two pointwise quantities as the Reynolds number is increased. In the Saffman model of reconnection, we found that the axial strain in the vortex core, $\partial w/\partial z$ in (1.13), behaved in a way practically independent of Reynolds number, while the vorticity ω showed a strong dependence upon the Reynolds number because its growth becomes unbounded in the infinite Reynolds number limit as $t \rightarrow \infty$ (see figure 4).

For $Re = 500$, the vorticity remained nearly constant for most of the calculation. This suggests a balance of stretching and dissipation reminiscent of a diffusing, circular vortex in a radial straining flow (Batchelor 1967, p. 271). The behaviour is

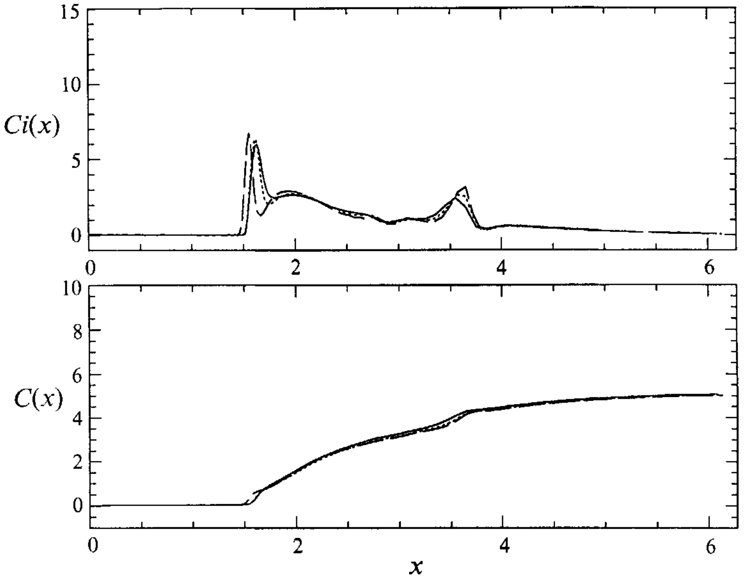

FIGURE 21. (*a*) The quantity $Ci(x)$ as a function of Re at $Re = 2000$ (solid curve), $Re = 2500$ (short-dashed), $Re = 3000$ (medium-dashed), and $Re = 3500$ (long-dashed). (*b*) The circulation $C(x)$ (see text) shown at the same values of Re. Both are at $t = 1.5$.

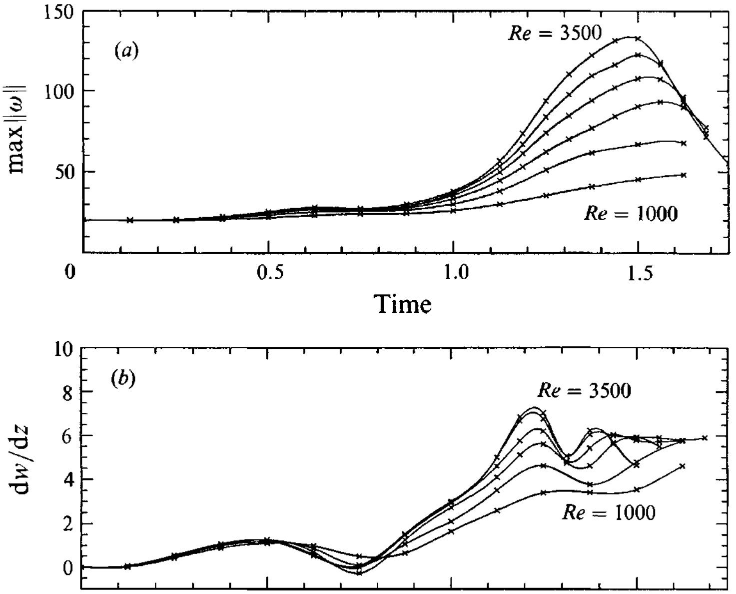

FIGURE 22. (*a*) The maximum of the vorticity in Π, i.e. ω_3, and (*b*) the axial strain $\partial w/\partial z$ at the point of maximum vorticity in Π for the Reynolds numbers 1000, 1500, 2000, 2500, 3000, and 3500.

very different with higher Reynolds numbers, for which such a balance is plainly not present. Initially, from $t = 0$ to 0.75, there is very little growth in the vorticity. It is only from this latter time that the vorticity maximum has become well correlated with positive axial strain, and both the axial strain and vorticity begin to grow. This delay in the realignment of the vorticity with positive axial strain, was also observed in the reconnection study of Meiron *et al.* (1989) using zero-circulation vortices.

As the Reynolds number is increased, the maximum value of ω_3 realized in the calculation is increased. This is not surprising as the vorticity is expected to grow without bound in the absence of viscosity as $t \rightarrow \infty$. However, the time at which this maximum value is realized actually decreases as the Reynolds number is increased. Referring to figure 4, we note that this behaviour is at variance with that predicted by the Saffman model as well as the simpler two-dimensional models, wherein the time at which the vorticity maximum is realized increases with increasing Reynolds number. On the other hand, the two highest Reynolds numbers, 3000 and 3500, peak at approximately the same time ($t \approx 1.5$), rather than showing any further decrease, which is perhaps an indication that this trend will reverse at higher Reynolds numbers.

Here we make several remarks. In the plane of closest approach the vorticity maximum does not coincide with the maximum of the axial strain rate $\partial w/\partial z$. Such a coincidence would presumably lead to a greater rate of stretching. This was also observed by Pumir & Siggia (1990) in their study of vorticity interactions. The axial strain $\partial w/\partial z$ has both positive and negative values in Π as a consequence of the incompressibility constraint, which implies that

$$\int_{\Pi} \frac{\partial w}{\partial z} \mathrm{d}A = 0.$$

The various models of vortex merger and cancellation discussed in §§1 and 2, posit strain fields with uniform rates of strain covering the vortex cores. It is clear from figure 16(*a–d*) that the axial strain rate $\partial w/\partial z$ is quite non-uniform. In fact, portions of the vortex sit within regions of negative strain. However, we note again that the vortex maximum and the vortex ribbons both sit within the region of positive strain. The asymmetry of the core deformation is typical of two compact vortices being driven together under the action of strain, and may not be important in determining the asymptotic timescales for reconnection. In their numerical study of two compact vortices being driven together under constant rates of strain, Buntine & Pullin (1989) observed very similar asymmetries and also found that the timescales for dissipation were still given by their generalization of Kambe's analysis. Additional discussion of the average rate of strain will be presented in the next subsection.

3.4.2. *Variation of the axial rate of strain*

The behaviour of the axial strain at the point of maximum vorticity is not quite so anomalous. While it is clear that there is a large dependence upon Reynolds number, there is the possible emergence of a limiting behaviour. Omitting the $Re = 1000$ case, we see that for each Reynolds number the axial strain begins to increase from $t = 0.75$. Then, before the time of the peak in the vorticity, $\partial w/\partial z$ itself attains a maximum and then apparently saturates. For the two highest Reynolds numbers, 3000 and 3500, the two curves are practically indistinguishable up to the time of the peak, at which they have a slight separation. This is consistent with the behaviour observed by Pumir & Siggia in their study of inviscid vortex interactions. If this behaviour is indicative of that at infinite *Re*, then growth of the maximum vorticity is at most exponential as pointed out by Pumir & Siggia (1990). We have performed a resolution check to ascertain that the behaviour of the strain is not an artifact of inadequate resolution. Shown in figure 23(*a*) is the axial strain at the point

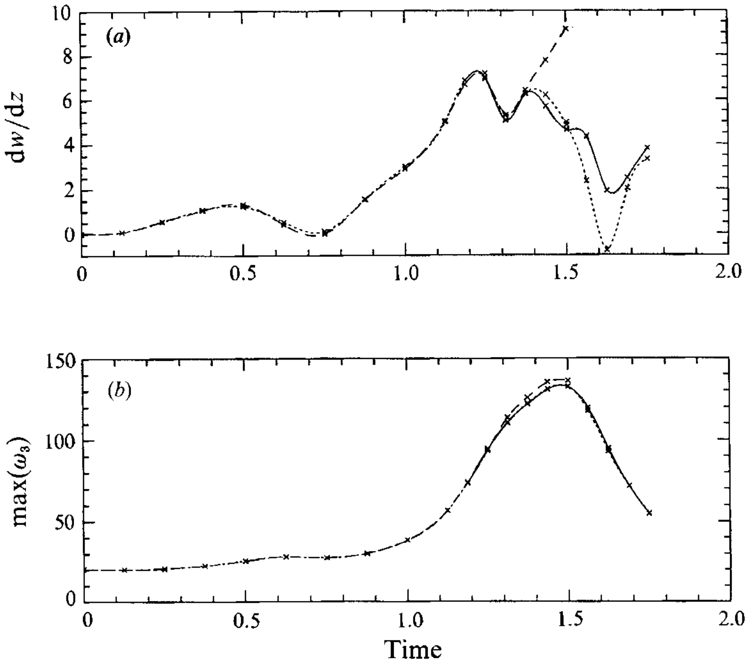

FIGURE 23. (*a*) The axial strain $\partial w/\partial z$ at the point of maximum vorticity in Π, and (*b*) the maximum vorticity in Π, for Reynolds number 3500 at various resolutions (96^3 (long-dash), 128^3(short-dash), and 160^3 (solid, from $t = 1.1875$)) on the whole cube.

of maximum vorticity for several resolutions (96^3, 128^3, and 160^3 (from $t = 1.1875$) on the whole cube). Likewise, figure 23(*b*) shows the maximum vorticity. The 96^3, 128^3, and 160^3 calculations all agree well up to $t = 1.375$, which is past the saturation time of the axial strain ($t \sim 1.22$). For the axial strain, the 128^3 and 160^3 calculations agree fairly well only up to about $t = 1.50$; in the maximum vorticity they agree well to $t = 1.75$. We found it typical that the axial strain at the point of maximum vorticity is a much more difficult quantity to capture well than the maximum vorticity itself. But, we conclude that at the resolutions used here, the saturation of the axial strain is a consistent result.

The behaviour of the maximum vorticity with increasing *Re*-may be thought to be indicative of a finite time singularity. However, we note from (3.26) that the vorticity maximum cannot diverge if the axial strain remains a bounded function in time. No apparent divergence is seen in the axial strain, but it is possible that the Reynolds number is not yet sufficiently large to have been truly asymptotic behaviour in this quantity.

3.4.3. *Assessment of the rate of strain*

Figures 24(*a*) and 24(*b*) show the position of the vorticity maximum in Π, $x_{\max}(t)$ and $y_{\max}(t)$. A measure of the translation of the vortices in the plane of closest approach is given by $x_{\max}(t)$. As the free-slip surface between the two vortices is located at $y = \pi$, the distance between the two symmetrically placed extrema is $2(\pi - y_{\max}(t))$. As the vortices are being driven together (cf. figure 22(*a*)), their area is decreased by stretching but there is little accompanying increase in the translational velocity owing to the flattening of the vortex cores. This behaviour is contrary to that observed in the circular filament calculations of Pumir & Siggia, wherein the translational velocity diverged as the cores were pushed together.

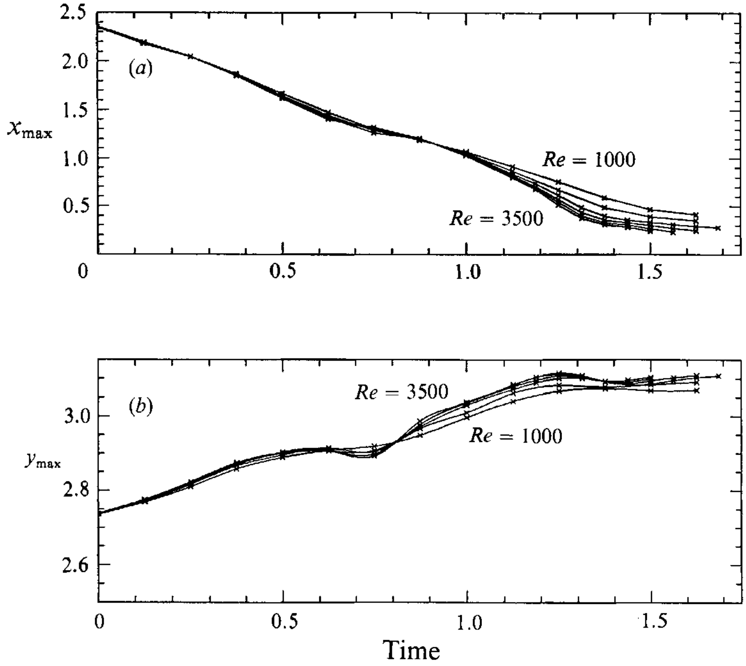

FIGURE 24. (*a*) The x-coordinate of the vorticity maximum in Π, and (*b*) the y-coordinate of the vorticity maximum in Π, as functions of time.

Indeed, the translational velocity of the vortices here appears to be decreasing near $t = 1.5$. It is well known that in two-dimensional flow the velocity of advance of two vortices of opposite sign is decreased if the vortices become very elliptical. It is easy to show analytically that the instantaneous velocity of advance of two Kirchhoff elliptical vortices of equal and opposite circulation evaluated at either vortex centroid is given by

$$u = \frac{\Gamma}{(b^2+a^2+l^2)^{\frac{1}{2}}+l},$$

where a and b are the minor and major semi-axes of the ellipse, respectively, and l is the inter-centroid separation. In a two-dimensional flow, if a decreases, then b must increase by conservation of area. If b becomes sufficiently large, then u becomes a decreasing function of increasing b. Of course, if this interpretation is applied to the present situation, we must note the area is not conserved (owing to the axial strain), and that both a and l are decreasing. Nonetheless, u in the above expression is bounded above by Γ/b, and b is bounded well away from zero (see below). This effect tends to reduce any further rapid stretching of the vortices due to translation.

One reflection of the straining flows is the deformation of the vortices in the plane of closest approach. Figure 25(*a*) shows an estimate of a (dashed) and b (solid), again the minor and major axis lengths of a vortex, as functions of time, for $Re = 3500$. Following Buntine & Pullin, these quantities were estimated by first- and second-moment calculations, performed over the main portion of the vortex. The behaviour of a and b is consistent with that seen in the vorticity contours of figure 15. Of most interest is the rapid saturation of b, the major axis length, together with the continuing decrease of a. This suggests that the extensional rate-of-strain $(-(\alpha+\beta) = \gamma$ in Saffman's model) has become small, and that the straining flows are now

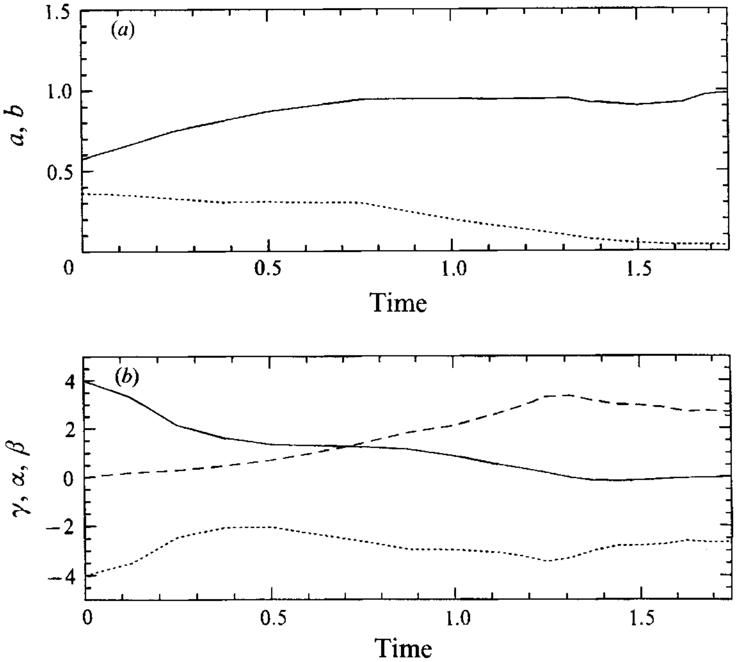

FIGURE 25. (*a*) The major and minor axis lengths a and b (dashed and solid, respectively) of the vortex core in Π, as functions of time for $Re = 3500$. (*b*) Averaged rates of strain, α (compressional, short-dashed), β (axial, long-dashed), and $\gamma = -(\alpha+\beta)$ (extensional, solid), as functions of time for $Re = 3500$.

dominated by the compressional and axial strains (α and β, respectively). This is contrary to the assumptions of the Saffman model, wherein b cannot saturate owing to the assumption of time-independence for α. We note that the estimates of a and b when $Re = 3000$ match very well with those for $Re = 3500$ to nearly $t = 1.50$. This may indicate that the behaviour of a and b is nearly inviscid up to this time. Further note that b is well away from zero, which suggests that rapid stretching through translation is controlled.

It is most natural to examine the straining flows in the plane of closest approach between the two vortices. In particular, the rate-of-strain matrix, S_{ij}, has its simplest form along the line of symmetry, $y = \pi$ in the plane of closest approach, which separates the two vortices. There S_{ij} has only diagonal terms, and thus the principal rates of strain are given by $\gamma(x) = (\partial u/\partial x)(\pi, \pi, x)$ (extensional), $\alpha(x) = (\partial v/\partial y)(\pi, \pi, x)$ (compressional), and $\beta(x) = (\partial w/\partial z)(\pi, \pi, x)$ (axial). To gain some understanding of the straining flows acting upon the vortices, these rates of strain are averaged in x over that portion of the line which begins and ends at the fore and aft of the vortex, respectively. Figure 25(*b*) shows these averaged quantities, for $Re = 3500$, as functions of time (α is dashed, β is long-dashed, and γ is solid). The behaviour of these quantities is consistent with that of a and b, and more clearly reveals the differences from the assumed straining flows of the Saffman model of reconnection. While the straining flow is initially two-dimensional, β grows rapidly, and as seen for the pointwise axial strain at the point of maximum vorticity, subsequently saturates. As suggested by the behaviour of b, the positive extensional rate of strain γ decreases and becomes small relative to the other two. Finally, the compressional rate of strain α is strongly time-dependent, and the final disposition of straining flows is quite different from that assumed in the Saffman model. Comparison of the rate-of-strain

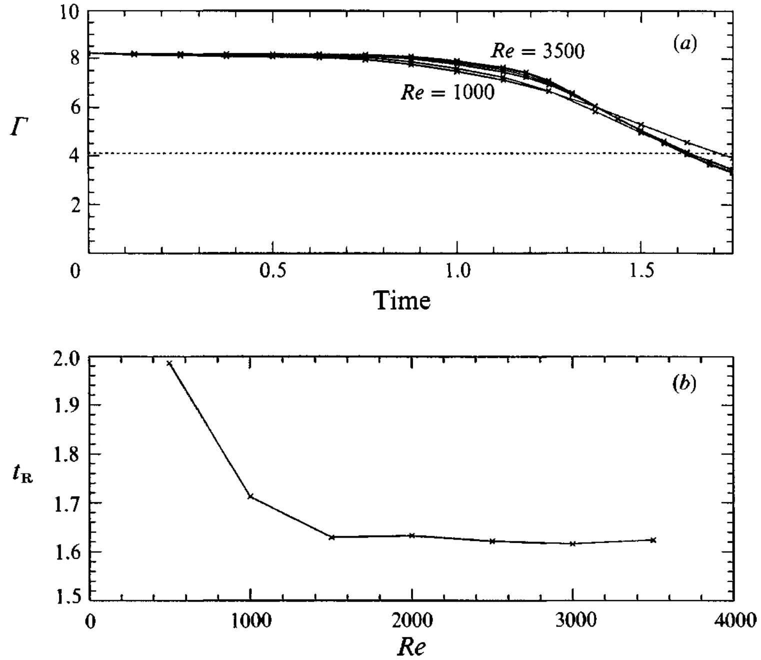

FIGURE 26. (*a*) The circulation C_Π as a function of time for $Re = 1000$, 1500, 2000, 2500, 3000, and 3500, and (*b*) the reconnection time t_R as a function of Reynolds number.

estimates for $Re = 3500$ shown in figure 5 agree very well with those for $Re = 3000$ up to and including $t = 1.75$.

3.4.4. *Variation of the time to reconnection with Reynolds number*

We next examine the reconnection time as a function of Reynolds number. Again we define, as in our discussion of the Saffman model, the reconnection time as the time required to decrease the initial circulation by a factor of two. Figure 26 (*a*) shows C_Π for the various Reynolds numbers. The dashed horizontal line is at half the value of the initial circulation, and the time at which it intersects a circulation curve defines the reconnection time t_R (cf. §2.3). This time is shown in figure 26 (*b*) as a function of Reynolds number ($Re = 500$ has also been included for comparison). For the higher Reynolds numbers, C_Π shows very little dependence on Re, and the curves become practically indistinguishable from one another after the circulation begins to decay appreciably. The results imply that the time for reconnection varies more slowly with Reynolds number than even the slow logarithmic variation suggested by present theory. It is, of course, possible that the largest value of Re considered here is still insufficient to observe the expected logarithmic variation. Another possible explanation is that the straining flows are not accounted for properly by the theory and their true behaviour leads to an even slower variation of the reconnection time with increasing Re.

4. Conclusions

We close with several comments with respect to points of agreement and disagreement with Saffman's reconnection model and its prediction. While phenomenological, Saffman's model qualitatively reproduces some of the aspects of the reconnection process. In particular, they are

(i) the presence of in-plane straining flows which drive the vortices together in the plane of closest approach, which through the resultant non-uniformity of the vortex tubes, creates axial flows which stretch the vortex;

(ii) the flattening of the vortex cores as they are pushed together. The effect of this flattening is included in the calculation of the axial flows;

(iii) the axial strain rate peaks at a maximum value, which slows the growth of the vorticity. In agreement with our calculations, it also predicts that the axial strain rate peaks before the peak in the vorticity occurs;

(iv) by including the effect of vortex flattening upon dissipation of the vorticity, it provides a fast timescale for reconnection.

Points of disagreement are that

(i) In Saffman's model, the axial strain rate ultimately decays in value like t^{-1}, which then gives a linear growth of the vorticity in the absence of viscosity. We do not observe this behaviour. Rather, the axial strain rate peaks, but does not subsequently decay. In Saffman's model, once the pressure gradient decays to zero there is no further axial strain to stretch the vorticity. In reality a flow is induced by the counter-rotating reconnected rings which will continue to stretch the vorticity, albeit passively.

(ii) Although the straining flows deforming the vortex are dominated by in-plane strain initially, at late times the straining flows are predominantly out of the plane of closest approach, with a compensating strain inwards which further flattens the vortices. There is little extensional component, however (see figure 26). In order to add this significant effect to the model it is necessary to couple the straining flows to the overall curvatures of the vortex tubes.

(iii) The most interesting result from these simulations is the apparently very slow variation of the reconnection time with *Re*. Although we have not been able to explore even a decade in *Re* relative to the initial value of $Re = 1000$ one would expect to see an increase in the reconnection time. The extremely slow variation exhibited here is also evident in the calculations of Kerr & Hussain (1989). Indeed, in their calculations using a Gaussian vorticity distribution, the reconnection time appears to decrease slightly. Their results are actually more in accord with a reconnection time arising from the Siggia–Pumir model whereas our results do indicate a slight increase of the reconnection time at the highest Reynolds number. The logarithmic variation of the reconnection time in the models of Kambe, Buntine & Pullin, and Saffman arises from the assumption of a constant underlying in-plane strain (α in Saffman's model equations). A more rapid increase of the axial or in-plane strains with time would lead to more rapid reconnection and a slower variation of the reconnection time. One such contribution to the axial strain, not accounted for in the Saffman model, would arise from the decay of C_{Π}. As circulation in Π is lost, it reappears as reconnected vortex lines crossing Π' (see figure 19). These reconnected vortex lines will exert an additional axial strain as they are advected upwards. Ultimately these vortex lines will form the section of vortex ring crossing Π', as seen in the volume renderings, figures 12 and 13. Again, that the disposition of the straining flow is not properly accounted for in Saffman's model is seen through examination of the contour plots of ω_3 in the plane of closest approach (figures 15 and 20), together with figure 25 which shows estimates of the vortex semi-axis lengths and of averaged rates of strain. While we have seen extreme flattening of the vorticity distributions, we have not seen as severe an elongation as is predicted by Saffman's model. This is due to the straining flows in the region of closest approach becoming dominated by the compressional and axial strain rate components. This may also have some effect on the variation of the reconnection time.

There are other proposed reconnection scenarios in the literature. In particular, Melander & Hussain (1988, p. 257) have provided a descriptive model illustrating how reconnected vortex lines straighten and accumulate only near the head of the vortex in the reconnection region (this feature is visible in the colour renderings). The mechanisms espoused by Saffman and by Melander & Hussain may be complementary. Saffman's model uses arguments about the tube non-uniformity and pressure to infer the existence of axial flows. A model also including Melander & Hussain's picture would presumably take into account the additional strain from the reconnected vorticity. In the light of the discussion above it would be of interest to construct a self-consistent model of reconnection which takes into account these apparently enhanced strains. This is currently under investigation.

Finally, it is interesting to note that the behaviour of the flow in the region of reconnection may not be typical of turbulent flows. Ashurst *et al.* (1987) have performed a statistical study of the alignment of vorticity and strain rates in Navier–Stokes turbulence. They found that vorticity, on average, tends to align itself not in the direction of the most negative or most positive rate of strain, but rather in the direction of the remaining, lesser rate of strain. From figure 25 we see instead that in the region of closest approach the vorticity becomes aligned with the most positive rate of strain. Boratav, Pelz & Zubusky (1992) have recently performed a careful numerical simulation of reconnection when the vortices are initially perpendicular and a different set of symmetries holds for the ensuing flow. In this case, they do observe the statistical alignments of the vorticity with the intermediate rate of strain.

We wish to thank Derek Moore, Andrew Majda, Dale Pullin, Jim Buntine, and especially Philip Saffman for valuable discussions and suggestions. We also wish to acknowledge the ambience of the Third Coast Café in Chicago where much of this work was done. This work was supported by the Department of Energy, Office of Energy Sciences (DE-AS03-76ER-72012), Applied Mathematical Sciences (KC-07-01-01), and by the Office of Naval Research under contracts N00014-85-K0205, N00014-82-C-0451, and N00014-86-K-0759. M.J.S. was supported by a NSF Mathematical Sciences postdoctoral fellowship.

REFERENCES

Anderson, C. & Greengard, C. 1989 The vortex ring merger problem at infinite Reynolds number. *Commun. Pure Appl. Maths* **42**, 1123.

Ashurst, W. T., Kerstein, A. R., Kerr, R. M. & Gibson, C. H. 1987 Alignment of vorticity and scalar gradient with strain rate in simulated Navier–Stokes turbulence. *Phys. Fluids* **30**, 2343.

Ashurst, W. T. & Meiron, D. I. 1987 Numerical study of vortex reconnection. *Phys. Rev. Lett.* **58**, 1632.

Batchelor, G. K. 1967 *An Introduction to Fluid Dynamics.* Cambridge University Press.

Beale, J. T., Kato, T. & Majda, A. 1984 Remarks on the breakdown of smooth solutions for the 3-D Euler equations. *Commun. Math. Phys.* **94**, 61.

Boratav, O. N., Pelz, R. B. & Zabusky, N. J. 1992 Reconnection in orthogonally interacting vortex tubes: Direct numerical simulations and quantifications. *Phys. Fluids* A **4**, 581.

Brachet, M., Meiron, D., Nickel, B., Orszag, S. A. & Frisch, U. 1983 The small-scale structure of the Taylor–Green vortex. *J. Fluid Mech.* **130**, 411.

Buntine, J. & Pullin, D. I. 1989 Merger and cancellation of strained vortices. *J. Fluid Mech.* **205**, 1632.

CANUTO, C., HUSSAINI, M. Y., QUARTERONI, A. & ZANG, T. A. 1988 *Spectral Methods in Fluid Dynamics.* Springer.

CHORIN, A. 1982 Evolution of a turbulent vortex. *Commun. Math. Phys.* **83**, 517.

CROW, S. 1970 Stability theory for a pair of trailing vortices. *AIAA J.* **8**, 2172.

FOHL, T. & TURNER, J. S. 1975 Colliding vortex rings. *Phys. Fluids* **18**, 433.

GOTTLIEB, D. & ORSZAG, S. A. 1977 *Numerical Analysis of Spectral Methods: Theory and Applications.* SIAM-CBMS.

GRAUER, R. & SIDERIS, T. 1991 Numerical computation of 3d incompressible fluids with swirl. *Phys. Rev. Lett.* **67**, 3511.

KAMBE, T. 1983 A class of exact solutions of two-dimensional viscous flow. *J. Phys. Soc. Japan* **52**, 834.

KERR, R. M. & HUSSAIN, A. K. M. F. 1989 Simulation of vortex reconnection. *Physica* D **37**, 474.

KIDA, S. 1987 Reconnection of vortex tubes. *Proc. IUTAM Symp. on Fundamental Aspects of Vortex Motion, Tokyo* (ed. H. Hasimoto & T. Kambe). North-Holland.

KIDA, S. & TAKAOKA, M. 1991 Breakdown of frozen motion fields and vorticity reconnection. *J. Phys. Soc. Japan* **60**, 2184.

LUNDGREN, T. S. & ASHURST, W. T. 1988 Area varying waves on curved vortex tubes with application to vortex breakdown. *J. Fluid Mech.* **200**, 283.

MEIRON, D., SHELLEY, M., ASHURST, W. T. & ORSZAG, S. A. 1989 Numerical studies of vortex reconnection. In *Mathematical Aspects of Vortex Dynamics* (ed. R. Caflisch). SIAM.

MELANDER, M. V. & HUSSAIN, F. 1988 Cut-and-connect of two antiparallel vortex tubes. *CTR Rep.* CTR-588, p. 257.

MELANDER, M. V. & HUSSAIN, F. 1989 Cross-linking of two antiparallel vortex tubes. *Phys. Fluids* A **1**, 633.

MELANDER, M. V., MCWILLIAMS, J. C. & ZABUSKY, N. J. 1987 Axisymmetrization and vorticity gradient intensification of an isolated two-dimensional vortex through filamentation. *J. Fluid Mech.* **178**, 137.

MELANDER, M. V. & ZABUSKY, N. 1987 Interaction and reconnection of vortex tubes via direct numerical simulations. In *Proc. IUTAM Symp. on Fundamental Aspects of Vortex Motion, Tokyo* (ed. H. Hasimoto & T. Kambe). North-Holland.

MELANDER, M. & ZABUSKY, N. 1989 Three dimensional vortex tube reconnection; morphology for orthogonally offset tubes. *Physica* D **37**, 555.

MOORE, D. W. & SAFFMAN, P. G. 1971 Structure of a line vortex in an imposed strain. In *Aircraft Wake Turbulence* (ed. J. Olsen, A. Goldberg & N. Rogers), p. 1. Plenum.

MOORE, D. W. & SAFFMAN, P. G. 1972 The motion of a vortex filament with axial flow. *Phil. Trans. R. Soc. Lond.* **272**, 403.

MORF, R. H., ORSZAG, S. A. & FRISCH, U. 1980 Spontaneous singularity in three-dimensional, inviscid, incompressible flow. *Phys. Rev. Lett.* **44**, 572.

OSHIMA, Y. & ASAKA, S. 1977 Interaction of two vortex rings along parallel axes in air. *J. Phys. Soc. Japan* **42**, 708.

PUMIR, A. & KERR, R. 1988 Numerical simulation of interacting vortex tubes. *Phys. Rev. Lett.* **58**, 1636.

PUMIR, A. & SIGGIA, E. D. 1990 Collapsing solutions to the 3-D Euler Equations. *Phys. Fluids* A **2**, 220.

SAFFMAN, P. G. 1990 A model of vortex reconnection. *J. Fluid Mech.* **212**, 395.

SCHATZLE, P. 1987 An experimental study of fusion of vortex rings. PhD thesis, Graduate Aeronautics Laboratory, California Institute of Technology.

SIGGIA, E. D. 1985 Collapse and amplification of a vortex filament. *Phys. Fluids* **28**, 794.

SIGGIA, E. D. & PUMIR, A. 1987 Vortex dynamics and the existence of solutions to the Navier–Stokes equations. *Phys. Fluids* **30**, 1606.

VAN DYKE, M. 1982 *An Album of Fluid Motion.* Stanford: Parabolic.